



HAL
open science

Impact of the porosity of an urban block on the flood risk assessment: A laboratory experiment

M.A. Mejia Morales, Emmanuel Mignot, André Paquier, Darius Sigaud,
Sébastien Proust

► To cite this version:

M.A. Mejia Morales, Emmanuel Mignot, André Paquier, Darius Sigaud, Sébastien Proust. Impact of the porosity of an urban block on the flood risk assessment: A laboratory experiment. *Journal of Hydrology*, 2021, 602, pp.126715. 10.1016/j.jhydrol.2021.126715 . hal-03573248

HAL Id: hal-03573248

<https://hal.science/hal-03573248>

Submitted on 7 Mar 2023

HAL is a multi-disciplinary open access archive for the deposit and dissemination of scientific research documents, whether they are published or not. The documents may come from teaching and research institutions in France or abroad, or from public or private research centers.

L'archive ouverte pluridisciplinaire **HAL**, est destinée au dépôt et à la diffusion de documents scientifiques de niveau recherche, publiés ou non, émanant des établissements d'enseignement et de recherche français ou étrangers, des laboratoires publics ou privés.

Author's version of the paper :

Mejía-Morales, M. A., E. Mignot, A. Paquier, D. Sigaud and S. Proust (2021).

"Impact of the porosity of an urban block on the flood risk assessment: A laboratory experiment."
Journal of Hydrology 602: 126715. DOI: 10.1016/j.jhydrol.2021.126715

Highlights

Impact of the porosity of an urban block on the flood risk assessment: a laboratory experiment

Miguel Angel Mejía-Morales, Emmanuel Mignot, André Paquier, Darius Sigaud, Sébastien Proust

- Physical modelling of urban flooding usually neglects flow exchanges between streets and urban blocks.
- We performed laboratory experiments to study the flow in and around an urban block with several openings.
- Eight cases were tested varying the number and locations of the urban block openings.
- In the streets surrounding the block, flow depth and velocity varies by up to 10% and 70%, respectively depending on the number of openings.
- The level of risk is modified mainly in the vicinity with the block openings, both in the streets and within the block.

Author's version of the paper :

Mejía-Morales, M. A., E. Mignot, A. Paquier, D. Sigaud and S. Proust (2021).

"Impact of the porosity of an urban block on the flood risk assessment: A laboratory experiment."

Journal of Hydrology 602: 126715. DOI: 10.1016/j.jhydrol.2021.126715

Impact of the porosity of an urban block on the flood risk assessment: a laboratory experiment

Miguel Angel Mejía-Morales^a, Emmanuel Mignot^b, André Paquier^a, Darius Sigaud^a, Sébastien Proust^a

^aUR RiverLy - INRAE, 5 rue de la Doua CS 20244 69625 Villeurbanne

^bLMFA - INSA Lyon, Université de Lyon, 20 avenue A. Einstein 69621 Villeurbanne

Abstract

Physical modelling of urban flooding usually considers that the flow is concentrated in the streets, assuming that urban blocks and individual buildings are non-porous structures. This assumption is open to criticism, as potential lateral flow exchanges through openings in the walls of an urban block (e.g. gates, windows and doors) are likely to modify the flow pattern in the block and adjacent streets. This paper reports an experimental study conducted on a 5.4 m long and 3.2 m wide physical model, representing a rectangular urban block and four surrounding streets. The focus of the study was on investigating the lateral flow exchange processes between the porous urban block and its adjacent streets during flooding for a variable urban block porosity. Eight porosity values were studied, keeping the same boundary conditions. A porosity equals zero, i.e. a flow around a non-porous block, served as a reference flow situation. For each porosity value, the impact of

Email addresses: miguel-angel.mejia-morales@inrae.fr (Miguel Angel Mejía-Morales), emmanuel.mignot@insa-lyon.fr (Emmanuel Mignot), andre.paquier@inrae.fr (André Paquier), darius.sigaud@inrae.fr (Darius Sigaud), sebastien.proust@inrae.fr (Sébastien Proust)

the lateral flow exchanges on the spatial distribution of the flow depth and velocity in the streets and within the block was assessed, as well as the risk for pedestrians. First, it was found that, in the streets surrounding the block, flow depth and depth-averaged velocity can vary by 10% and 70%, respectively, when modifying block porosity. Within the block, the most impacted flow parameter is the number and size of horizontal secondary flow cells. Second, noticeable differences in flow depth can be observed from either side of an opening between street and block. Third, when moving away from the block, flow parameters are little affected. Last, the risk to pedestrians, which is both related to local flow depth and velocity, is dependent on the block porosity value.

Keywords: laboratory experiment, urban flood risk, urban block porosity, LSPIV technique

1. Introduction

According to UNISDR et al. (2015), flood events increased by 39% from 2004 to 2013 with respect to the previous decade. The damage to goods and people caused by these events is particularly significant in urban settlements, mainly because of the high population density and the value of the assets. As reported by United Nations et al. (2019), the number of people living in urban areas worldwide is increasing, and it is estimated that, by 2050, it will be the case for two thirds of the world's population. Therefore, developing methodologies to assess the urban flood hazard and the associated risk with higher precision is particularly relevant.

Flood hazard is usually described by flow depth, flood extent, flow ve-

12 locity, flood wave propagation, flood duration and the water’s rising rate
13 (de Moel et al., 2009). Among these, the most common parameters are
14 the local velocity and flow depth, used for the prediction of building dam-
15 age (e.g. Jakob et al., 2012; Lo et al., 2012; Maiwald and Schwarz, 2012;
16 Milanesi et al., 2018), instability of parked and transit vehicles (e.g. Shu
17 et al., 2011; Xia et al., 2011, 2014b; Teo et al., 2012; Kramer et al., 2016;
18 Martínez-Gomariz et al., 2017; Gómez et al., 2018), and people’s instabil-
19 ity (e.g. Karvonen et al., 2000; Jonkman and Penning-Rowsell, 2008; Russo
20 et al., 2013; Chanson et al., 2014; Xia et al., 2014a; Milanesi et al., 2016;
21 Martínez-Gomariz et al., 2016; Arrighi et al., 2017, 2019).

22 Urban flood studies are then more often conducted to quantify the spatial
23 distribution of velocity and flow depth to establish flood hazard and risk
24 maps (e.g. Chen et al., 2019; Costabile et al., 2020; Galuppini et al., 2020).
25 However, studying flood events in an urban environment remains a challenge,
26 because it requires incorporating various topographical details in the flooding
27 model (e.g. buildings, street furniture and vehicles, sewage system, subway),
28 and the latter must account for the complex interplay between flow and
29 topographical and hydraulic singularities (e.g. interaction with fixed and
30 mobile obstacles, streets-sewer network or streets-buildings flow exchanges).
31 Among the tools used to study these events, numerical modelling is the
32 most widely used method, especially two-dimensional (2-D) modelling (e.g.
33 Mignot et al., 2006; Soares-Frazão et al., 2008; El Kadi Abderrezzak et al.,
34 2009; Guinot, 2012; Bazin et al., 2017), since: (i) flows within the urban
35 area are too complex for 1-D models; (ii) the involved horizontal geometrical
36 length-scales are often large compared to flow depths; and (iii) studies using

37 3-D modelling demand a high computational cost (Paquier et al., 2019).
38 However, the scarcity of detailed and reliable data on real-world urban flood
39 events represents a drawback to the calibration and validation of these models
40 (Macchione et al., 2019). In this context, laboratory physical models are a
41 convenient alternative, especially useful, for investigating flow patterns in
42 complex geometries under controlled conditions (Finaud-Guyot et al., 2018).
43 They can provide reliable information and detailed observations at local scale,
44 and can also be used as a benchmark tool for the calibration of numerical
45 models.

46 Although real-world urban blocks and individual buildings include open-
47 ings (e.g. doors, windows, gates, fences) and interior spaces (e.g. gardens,
48 courtyards, parking lots), most experimental urban flood studies consider
49 them as non-porous structures through which the flow cannot enter (e.g.
50 Ishigaki, 2003; Araud et al., 2014; Finaud-Guyot et al., 2018). However, to
51 the best of the authors' knowledge, no study has proved that the impact
52 of the exchanges between the street network and urban blocks on the flow
53 characteristics is negligible, and accordingly, has to be discarded. In general
54 terms, very few studies are dedicated to the flows entering buildings during
55 floods, except for the study of Zhou et al. (2016), who represented buildings
56 as square aligned and staggered obstacles, over a plain, with square open
57 windows, and the study of Sturm et al. (2018), who represented them as
58 real-world building shapes, over a floodplain, with open windows and doors.

59 As the lateral flow exchanges between urban blocks and streets have been
60 little studied, we took a closer look on these physical processes based on a lab-
61 oratory experiment. It was conducted using a tilting physical model termed

62 MURI (Maquette Urbaine pour l'étude du Risque d'Inondation, i.e. urban
63 model for the study of flood risk), at the Hydraulics and Hydro-morphology
64 Laboratory of INRAE centre Lyon-Villeurbanne, France (Figure 1.A). The
65 focus was on the exchanges between one single porous urban block and four
66 adjacent streets (Figures 1.B and 1.C). The openings in the urban block
67 walls stand for wide gates. Eight values of porosity were studied, including a
68 reference flow situation with a porosity equal to zero. The main aim was to
69 assess the impact of a variable block porosity on flow depths, velocities and
70 flow patterns in the streets and block, and on the lateral discharges through
71 each opening. Risk maps for pedestrians in the streets and block were then
72 deduced from the flood hazard assessment. Section 2 outlines the exper-
73 imental methodology including the description of the physical model, the
74 measurement techniques, the flow cases studied, and the flood risk criterion
75 for pedestrians. Section 3 reports the impact of porosity on the measured
76 flow features (water depth and velocity, exchange discharges, horizontal sec-
77 ondary flow cells). Section 4 discusses its impact on the related flood risk
78 to pedestrians inside the block and in the neighbouring streets. The main
79 conclusions are eventually drawn in section 5.

80 **2. Methodology**

81 *2.1. Experimental set-up*

82 The physical model for the study of flood risk, termed MURI, is a 5.4
83 m long and 3.8 m wide rectangular tilting platform, which comprises three
84 longitudinal streets and three transverse streets, and represents an urban
85 district (Figure 1.A). For this study, the working zone was reduced to 5.4 m

86 $\times 3.2$ m, focusing on a single 1.56 m long and 0.96 m wide rectangular block
 87 and four surrounding streets (upstream, downstream, right and left) of equal
 88 width, $b = 0.15$ m (Figures 1.B and 1.C), with two discharge inlets (upstream
 89 end of the right and left streets) and 4 discharge outlets (downstream end of
 90 all streets). The sidewalls of the block and streets are made of transparent
 91 plastic and the platform bed is made of grey PVC. The model bed slope in the
 92 longitudinal direction (aligned with the x -axis), S_{0_x} , was set at 0.12%, and
 93 the slope in the lateral direction (aligned with the y -axis), S_{0_y} , at zero. No
 94 building or furniture was placed within the block to maximize any potential
 95 flow through it. The porosity of the urban block walls was varied by changing
 96 the number of openings along them (with a maximum of three in each wall).
 97 Each opening was 6 cm wide and 8 cm high, and the free-surface flow always
 98 remained below the opening top.

99 The total inlet discharge, $Q_{in_T} = 6.5 \text{ ls}^{-1}$, was partitioned between the
 100 inflow in the right ($Q_{in_1} = 4.5 \text{ ls}^{-1}$) and left ($Q_{in_2} = 2.0 \text{ ls}^{-1}$) streets, as
 101 shown in Figure 1.C. Each inlet discharge was adjusted with an independent
 102 valve-flowmeter system, with a standard error of 3% of the flow rate. A
 103 honeycomb plastic grid was placed at the entrance of each street to straighten
 104 out the flow. At the outlet of each street, the flow fell into an outlet tank,
 105 the outlet discharge was then monitored using an electromagnetic flowmeter
 106 (OPTIFLUX 2000 by KROHNE). The four outlet discharges are denoted as
 107 Q_{out_1} , Q_{out_2} , Q_{out_3} and Q_{out_4} as depicted in Figure 1.C. At the downstream
 108 end of each street, a vertical tail weir enables flow depths in the street network
 109 to be controlled. In the present study, the weir heights were set to get a
 110 higher flow depth in the right street than in the left street, making easier a

111 transverse flow through the porous block (the weir height $w = 4$ cm at outlet
112 1, while $w = 3$ cm at outlets 2, 3 and 4).

113 The scale ratio in the horizontal plane, λ_{xy} , equals 50, and the vertical
114 scale ratio, λ_z , equals 10. The model then represents in the real-world an
115 urban block of $78.0 \text{ m} \times 48.0 \text{ m}$ and 7.5 m wide streets, with 3 m wide gates,
116 and flow depths of about 0.60 m . This difference in scale ratios leads to a
117 distorted-scale model with a distortion ratio $\lambda_{xy}/\lambda_z = 5$, which ensures: i)
118 greater flow depths, allowing greater accuracy during measurements, and ii)
119 larger Reynolds numbers, improving the dynamic similarity with the proto-
120 type (Chanson, 2004).

121 *2.2. Measuring techniques*

122 To answer all questions raised in section 1, the measuring devices had
123 to be set to access: (i) the flow depth fields in the streets and within the
124 urban block, (ii) the discharge within each street reach, (iii) the discharge
125 entering or leaving the urban block through each opening and (iv) the velocity
126 field over the whole measuring domain. Following subsections detail the
127 corresponding measurement methods.

128 *2.2.1. Flow depth*

129 The 2-D field of flow depth, d , was obtained using an Ultrasonic distance-
130 measuring Sensor (US), with an accuracy better than 0.3 mm and repro-
131 ducibility better than 0.5 mm (BAUMER UNDK 20I6914/S35A). The esti-
132 mated flow depth uncertainty equals 0.65 mm . The US is fixed on a mechan-
133 ical gantry system moving along both longitudinal (x -axis) and transverse
134 (y -axis) directions. Each measurement was taken at a sampling rate of 50 Hz

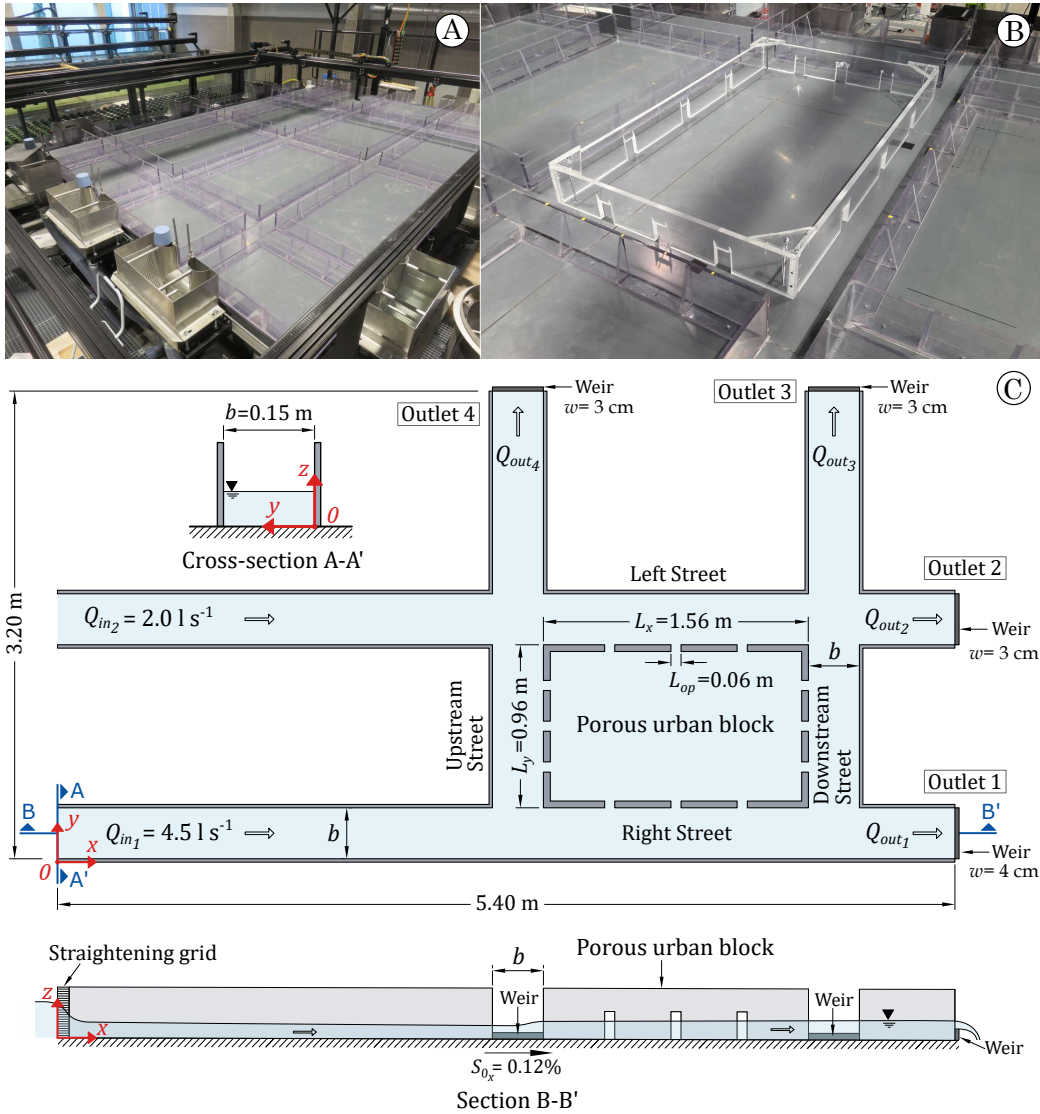


Figure 1: (A) General overview of the urban model for the study of flood risk, MURI (B) Zoom on the urban block with adjustable porosity (in picture the largest possible porosity). (C) Sketch and dimensions of the experimental set-up with the largest possible porosity, i.e. with 12 openings, as for case C19-12 (top and side view).

135 for 50 s (time convergence tests were carried out to define the appropriate
136 acquisition duration, see Appendix A.1). The spatial interval between two
137 measurements in the streets was equal to 5.0 cm and 6.5 cm in the stream-
138 wise and spanwise directions (3 measurements in the street cross-section),
139 respectively, and around 12.0 cm along both directions within the urban
140 block.

141 2.2.2. Velocity

142 The flow velocity in the water column was measured using an Acoustic
143 Doppler Velocimeter (ADV) with a side-looking probe (NORTEK Vectrino
144 +). Its accuracy is of 0.5% of the measured value. The three instantaneous
145 velocity components (u_x, u_y, u_z) were measured at each point at a sampling
146 rate of 100 Hz for 100 s in the streets and 200 s within the urban block. These
147 acquisition durations were defined based on time convergence tests of the
148 ADV' signal, under various flow conditions, as presented in Appendix A.2.
149 Water was seeded with polyamide powder (VESTOSINT[®]), with an average
150 particle diameter of 55 μm to increase the signal-to-noise ratio. The WinADV
151 software was used to process the ADV raw data, including a filtering step
152 based on the despiking technique proposed by Goring and Nikora (2002). The
153 sampling standard errors for the time-averaged local velocity components,
154 U_x , U_y and U_z are 0.20 cm s^{-1} ($\sim 0.4\%$), 0.06 cm s^{-1} ($\sim 1.5\%$) and 0.10
155 cm s^{-1} ($\sim 3.7\%$), respectively in the streets (these errors were estimated
156 based on 20 times series of 100 s each at the same measuring point at 3
157 different locations), and 0.13 cm s^{-1} ($\sim 2.0\%$), 0.05 cm s^{-1} ($\sim 23.3\%$) and
158 0.04 cm s^{-1} ($\sim 10.5\%$), respectively within the urban block (20 times series
159 of 200 s at 1 location).

160 The surface velocity in the streets and within the block was measured
161 using the Large Scale Particle Image Velocimetry technique (LSPIV). In
162 previous studies, this technique proved to be reliable for a laboratory use
163 (e.g. Muste et al., 2000; Kantoush et al., 2011), being able to accurately
164 measure small velocities in shallow-depth flows (Meselhe et al., 2004), and to
165 properly distinguish large-scale and small-scale flow structures (Fujita et al.,
166 1998). Wood shavings with diameters ranging from 1 to 4 mm were used
167 as free-surface tracers. This light and pale material sharply contrasted with
168 the dark grey colour of the model bed. A video camera (Panasonic, HC-
169 V770) was placed 2.8 m above the experimental set-up, with the optical
170 axis perpendicular to the model bed. The spatial resolution of the camera
171 was $1920 \text{ px} \times 1080 \text{ px}$, with a recording rate of 25 frames per second. In
172 addition to natural light, four led lamps with an adjustable light intensity
173 were used along with light diffusion screens to light up the set-up. The free
174 Fudaa-LSPIV software co-developed by EDF/INRAE was used to process
175 the videos and compute the time-averaged surface velocities. The required
176 recording duration was 60 s (see time convergence tests of the 2-D distribution
177 of time-averaged velocity in Appendix A.3).

178 It should be mentioned that seeding the flow at only one location to mea-
179 sure surface velocities over the entire domain was found to be inappropriate.
180 In this case, a large seeding generates clogging in small velocity areas and
181 along the main streets, while a limited seeding does not deliver sufficient
182 tracers in the upstream (transverse) street and within the urban block. The
183 best procedure arising from preliminary tests was actually to perform various
184 videos with different seeding locations for a given flow case (a procedure only

185 possible under steady flow conditions). Seeding the flow at the entrance of
186 the right and left streets, a first video recorded the tracer movements in the
187 right, left and downstream streets. Seeding at the entrance of the upstream
188 street, a second video recorded the tracers in this street. Last, seeding the
189 flow near the block openings (on the street side), a third video was taken to
190 measure surface velocity within the urban block. Application of the LSPIV
191 technique was then performed in each of these three areas independently,
192 and the resulting surface velocities were finally plotted on the same map.
193 The agreement in velocity magnitude and velocity direction at the intersec-
194 tions of the three zones gave confidence in the quality of the surface velocity
195 measurement.

196 Finally, to validate the surface velocity results, the velocity measured by
197 LSPIV was compared to ADV velocity. Two types of ADV velocity data
198 were considered here: near-surface velocities and depth-averaged velocities.
199 Within the block, the fair agreement of the LSPIV velocities with these two
200 types of ADV velocity data proves that flow is mainly two-dimensional (see
201 figure B.16 in Appendix B). In the streets, although velocity magnitude and
202 recirculating flow areas are adequately captured by LSPIV, the results in
203 some areas near the crossroads appear to be less accurate, mainly due to the
204 presence of strong flow depth fluctuations. In addition, the slight decrease in
205 velocity when approaching the walls in some areas was not observed either
206 (see figure B.17 in Appendix B). Overall, the velocities obtained with the
207 LSPIV technique in the streets are slightly lower than the near-surface ADV
208 data, mainly due to the clogging of the tracers. A video of the tracers' motion
209 used for LSPIV will be available on a web site before publication.

210 *2.2.3. Discharge*

211 The flow velocity within the water column was measured at 9 to 10 el-
212 evations (depending on flow depth) and at 15 lateral positions across the
213 wetted area in a street. The discharge in a street reach was then computed
214 by integrating the ADV velocity data across the street as follows:

$$Q_{st} = \int_0^b \int_0^d U_x dz dy, \quad \text{for } x\text{-axis-oriented streets} \quad (1)$$

or

$$Q_{st} = \int_0^b \int_0^d U_y dz dx, \quad \text{for } y\text{-axis-oriented streets} \quad (2)$$

215 where Q_{st} is the discharge in the street reach, U_x and U_y are the local time-
216 averaged velocity components along the x -axis and y -axis, respectively. We
217 should keep in mind that the inlet and outlet discharges were measured in
218 the pumping loop system using electromagnetic flowmeters. Then, based on
219 the mass conservation law at each crossroad and each opening, the number
220 of cross-sections over which the discharge had to be computed by Equation 1
221 or 2 from the ADV data was set just sufficient to assess the discharge within
222 each street reach and through each opening. Additional cross-sectional ADV
223 measurements were performed to compute discharges (with Eq. 1 or 2) and
224 verify that they were in agreement with discharges obtained using the mass
225 conservation law.

226 While the velocity field was measured as close as possible from the bed,
227 lateral walls and free-surface, areas along all four boundaries of a street cross-
228 section remained blind with no available velocity measurement. To estimate
229 the discharge in Equation 1 or 2, an extrapolation of the measured velocity
230 field was thus required with a slip condition applied at the free-surface and

231 a no-slip or an average between slip and no-slip conditions applied along the
232 bed and lateral walls (for details, see Appendix C).

233 Finally, it should be reminded that the estimate of the discharge at a given
234 cross-section in a street network remains a challenging task, even though
235 innovative techniques tend to arise (Finaud-Guyot et al., 2019). Preliminary
236 tests were conducted to compare the discharge estimated by Equation 1 or
237 2 with the discharges measured by the electromagnetic flowmeters, located
238 upstream of the inlet tanks and downstream of the outlet tanks, obtaining an
239 average error of 1.5%. Therefore, although the method requires assumptions
240 to cover the blind zones near the boundaries (bed, walls and flow surface), as
241 well as the inconvenience of using an intrusive instrument (ADV) in a narrow
242 cross-section, the results seem to be fairly reliable.

243 *2.3. Flow conditions and experimental cases*

244 The experiments were conducted under steady flow conditions and sub-
245 critical regime. The hydraulic boundary conditions, i.e., inflow discharges
246 and heights of the tail weirs, were kept constant from one porosity value to
247 another.

248 The porosity along each wall was defined as:

$$\psi = \frac{N \cdot L_{op}}{L_i}; \quad i = \{x, y\} \quad (3)$$

249 where ψ is the wall porosity, N is the number of openings along the wall, L_{op} is
250 the length of the opening and L_i is the total length of the wall. The flow cases
251 and the associated porosity values are reported in Table 1. Only symmetrical
252 distributions of the wall porosity were considered: the same value along right

253 and left streets; and the same along the upstream and downstream streets.
 254 The case C00-00 with a non-porous block, as mostly considered by previous
 255 works in the literature, serves as a reference flow situation. The extreme case
 256 100-100, without urban block, represents an urban configuration of a main
 257 square. In between, a small porosity (a single opening along a wall) and a
 258 large porosity (three openings along a wall) are both studied with six cases
 259 featuring the same porosity along face-to-face walls, along x -axis direction
 260 (C00-04 and 00-12), y -axis direction (C06-00 and C19-00), and finally along
 261 both directions (C06-04 and C19-12).

Table 1: Values of the wall porosity ψ (Eq. 3), and number of openings along each wall, N , for the eight flow cases.

Case	Upstream & Downstream walls		Right & Left walls	
	N	ψ (%)	N	ψ (%)
C00-00	0	0	0	0
C100-100	-	100	-	100
C00-04	0	0	1	4
C00-12	0	0	3	12
C06-00	1	6	0	0
C19-00	3	19	0	0
C06-04	1	6	1	4
C19-12	3	19	3	12

262 *2.4. Risk criterion for pedestrians*

263 For each flow case, the local flow depth and depth-averaged velocity to-
264 gether (hazard) with the vulnerability of pedestrians to flooding enable the
265 risk level to be assessed. The vulnerability was determined based on the
266 Product Number, $PN = Ud$, where U is the depth-averaged velocity magni-
267 tude and d the flow depth.

268 Over the past 50 years, several studies have been conducted with real
269 people to estimate their threshold of instability in flood flows (e.g. Foster
270 and Cox, 1973; Takahashi et al., 1992; Karvonen et al., 2000; Jonkman and
271 Penning-Rowsell, 2008; Russo et al., 2013; Martínez-Gomariz et al., 2016),
272 with real people and using a concrete monolith representing a real-size per-
273 son (e.g. Abt et al., 1989), using scale models (e.g. Xia et al., 2014a), which
274 is a more conservative approach that may well represent the lower limit of
275 people’s stability, or by observations made during real flood events (e.g. Mi-
276 lanesi et al., 2016). The results of each study showed a significant scatter,
277 and this was of course expected, as the instability threshold can be influ-
278 enced by many parameters defining human beings (e.g. the weight, height,
279 age, strength, skills, psychological characteristics), as well as the conditions
280 (e.g. experimental set-up, protective equipment, clothing of subjects) and
281 methodology (e.g. subject standing or walking, criteria for instability) car-
282 ried out in the various studies.

283 Cox et al. (2010) proposed vulnerability curves based on people instability
284 data sets available at that time. However, in the last 10 years additional
285 studies have been carried out, mainly exploring conditions of instability in
286 shallow flow with high velocities, common during floods in urban areas (e.g.

287 Russo et al., 2013; Xia et al., 2014a; Martínez-Gomariz et al., 2016). These
288 studies, as well as experiences acquired and observations made by Chanson
289 et al. (2014), suggest that the people’s instability in urban areas during floods
290 begins at lower flow depths and velocities than those reported in previous
291 studies. Therefore, following a procedure similar to that performed by Cox
292 et al. (2010), a new criterion of the risk to pedestrians during flooding in
293 urban areas is proposed based on the available experimental data and field
294 observations on people’s instability, and on various guidelines for the safety
295 of people during flooding.

296 Three Product Number thresholds are proposed: first, $PN = 0.3 \text{ m}^2 \text{ s}^{-1}$,
297 defines the lower limit of people’s stability according to Xia et al. (2014a)
298 and Abt et al. (1989) (results obtained using the concrete monolith), up to
299 $d = 0.7 \text{ m}$, based on the curve for critical self-evacuation proposed by Ishi-
300 gaki et al. (2009) and up to $U = 2.0 \text{ m s}^{-1}$, based on the limit of people’s
301 stability at small flow depths found by Russo et al. (2013) and Martínez-
302 Gomariz et al. (2016); second, $PN = 0.7 \text{ m}^2 \text{ s}^{-1}$, is the upper limit of Xia
303 et al. (2014a) results and where the first signs of people’s instability begin
304 for studies conducted by Abt et al. (1989), Takahashi et al. (1992) and Kar-
305 vonen et al. (2000), up to $d = 0.9 \text{ m}$ and up to $U = 2.70 \text{ m s}^{-1}$, which
306 represents approximately the mid-point in the range of velocities found for
307 people’ instability at small flow depths found by Russo et al. (2013) and
308 Martínez-Gomariz et al. (2016); and third, $PN = 1.0 \text{ m}^2 \text{ s}^{-1}$, corresponds to
309 approximately the 50% limit of instability cases of the total data set, up to d
310 $= 1.2 \text{ m}$, proposed by Cox et al. (2010), being the largest flow depth tested
311 in the available data series, and up to $U = 3.5 \text{ m s}^{-1}$, which is approximately

312 the upper limit of people’s stability at shallow flow according to Russo et al.
 313 (2013) and Martínez-Gomariz et al. (2016), i.e. above this limit almost all
 314 pedestrians exhibit instability. All these vulnerability curves are shown in
 315 the flood risk diagram for pedestrians, Figure 2, and they define four flood
 316 risk levels, which are as follows:

- 317 • *Low*, very few pedestrians exhibit instability (up to 2% of the total data
 318 set).
- 319 • *Moderate*, some pedestrians exhibit instability (up to 20% of the total
 320 data set).
- 321 • *Significant*, many pedestrians exhibit instability (up to 50% of the total
 322 data set).
- 323 • *High*, most pedestrians exhibit instability (above 50% of total data set).

The estimate of the local level of risk for pedestrians requires to firstly pass the results from the physical model scale to the real-world prototype scale, using Froude similarity, $Fr_m = Fr_p$ (Chanson, 2004; Heller, 2011), we have the following ratios:

$$\frac{U_p}{U_m} = \lambda_z^{\frac{1}{2}} \quad \text{for velocity} \quad (4)$$

$$\frac{d_p}{d_m} = \lambda_z \quad \text{for flow depth} \quad (5)$$

324 where subscripts m and p correspond to the model and the prototype respec-
 325 tively.

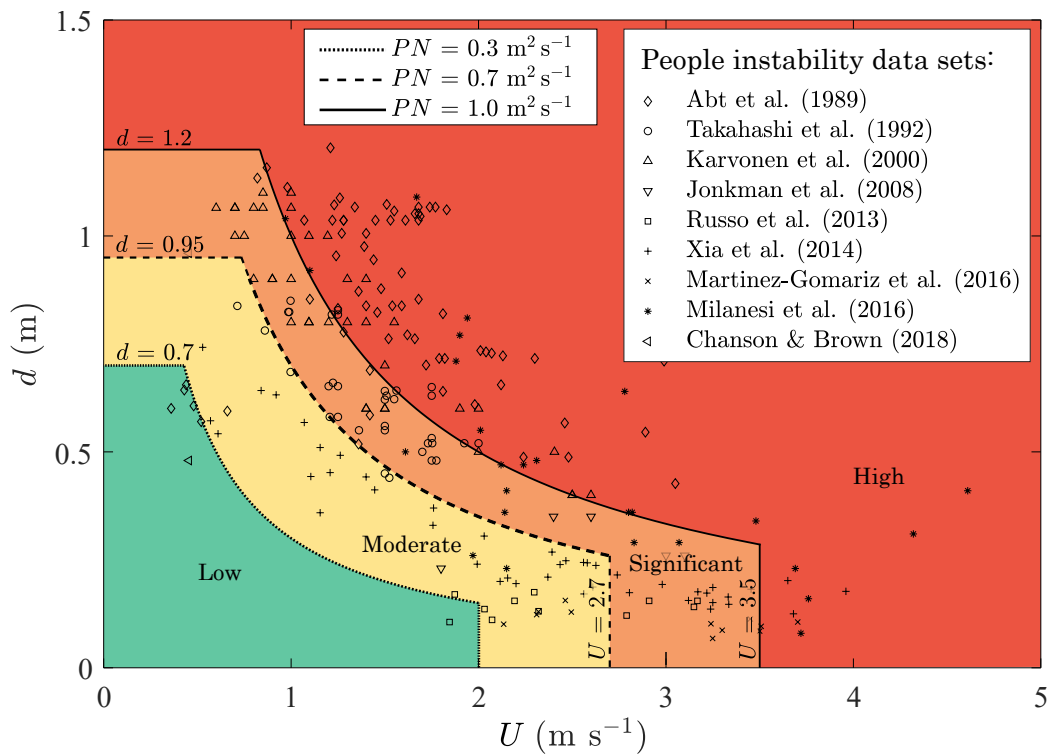


Figure 2: Proposed flood risk diagram as a function of the product number, $PN = Ud$, defining four levels of risk for adult pedestrians. Based on available experimental data and field observations on people instability, and recommended guidelines for the safety of people during floods.

326 **3. Measured flow features**

327 *3.1. Flow depth*

328 Figure 3 shows the spatial distribution of flow depth, d , in the streets and
329 urban block for all cases. Putting aside the case without block (C100-100),
330 the flow depth ranges from 5 cm to 7.5 cm (0.50 m - 0.75 m in the prototype)
331 for all flow cases. The largest flow depths are observed in the right street,
332 due to both the high inflow discharge in this street and the backwater effect
333 due to the 4 cm high tail weir located at the outlet of this street (Figure
334 1.C.). Inside the urban block, as the free-surface is almost horizontal, the
335 flow depth slightly increases along the x -axis due to the longitudinal bed
336 slope of the model.

337 Interestingly, the flow depth within the urban block can differ from the
338 flow depth in the adjacent streets. In the right street, the flow depth is
339 higher than in the block (up to 10% at $x = 3.25$ m for cases with a porosity
340 along the upstream and downstream block walls only, i.e. cases C06-00 and
341 C19-00). In contrast, the flow depth can be smaller in the downstream street
342 than in the block, e.g. by 14% at $y = 0.30$ m for cases with a porosity along
343 the right and left block walls only (C00-04 and C00-12).

344 Figure 4 shows the relative difference in flow depth, Δd , for each case
345 with respect to the reference case (C00-00), defined as:

$$\Delta d = \frac{d - d_{ref}}{d_{ref}} \times 100 \quad (6)$$

346 where d_{ref} refers to the flow depth of the reference case, C00-00. In the streets
347 surrounding the urban block, the relative difference in flow depth, Δd , can
348 reach up to -7% in the right street and 12.5% in the downstream street (case

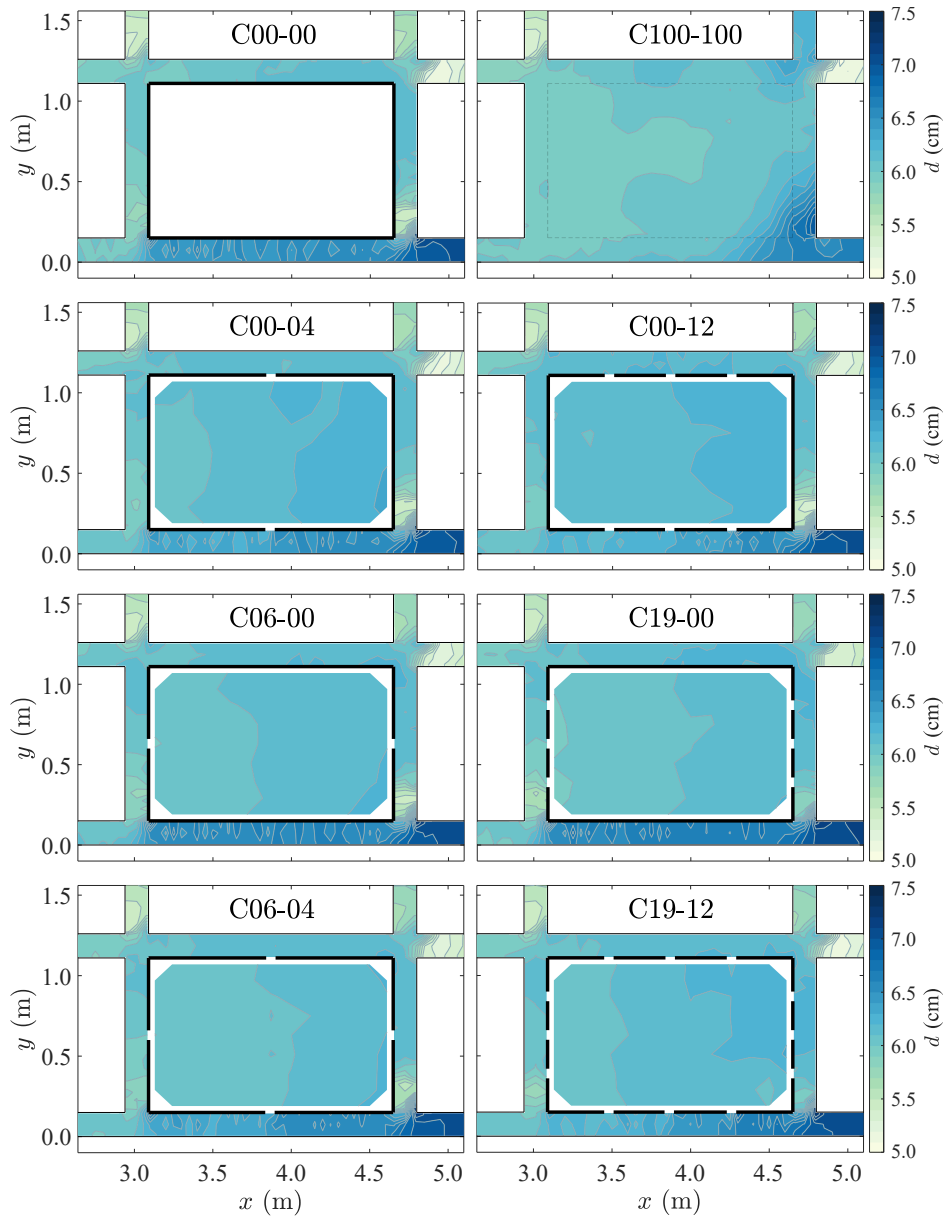


Figure 3: Flow depth d in the streets and within the urban block for all flow cases.

349 C19-12). In contrast, when moving away from the block, flow depths in the
 350 street reaches located upstream and downstream of the block (for $x < 2.94$
 351 m, $x > 4.80$ m and $y > 1.26$ m) do not show significant variations with
 352 respect to the reference case, with a maximum of 3.5 % (case C19-00).

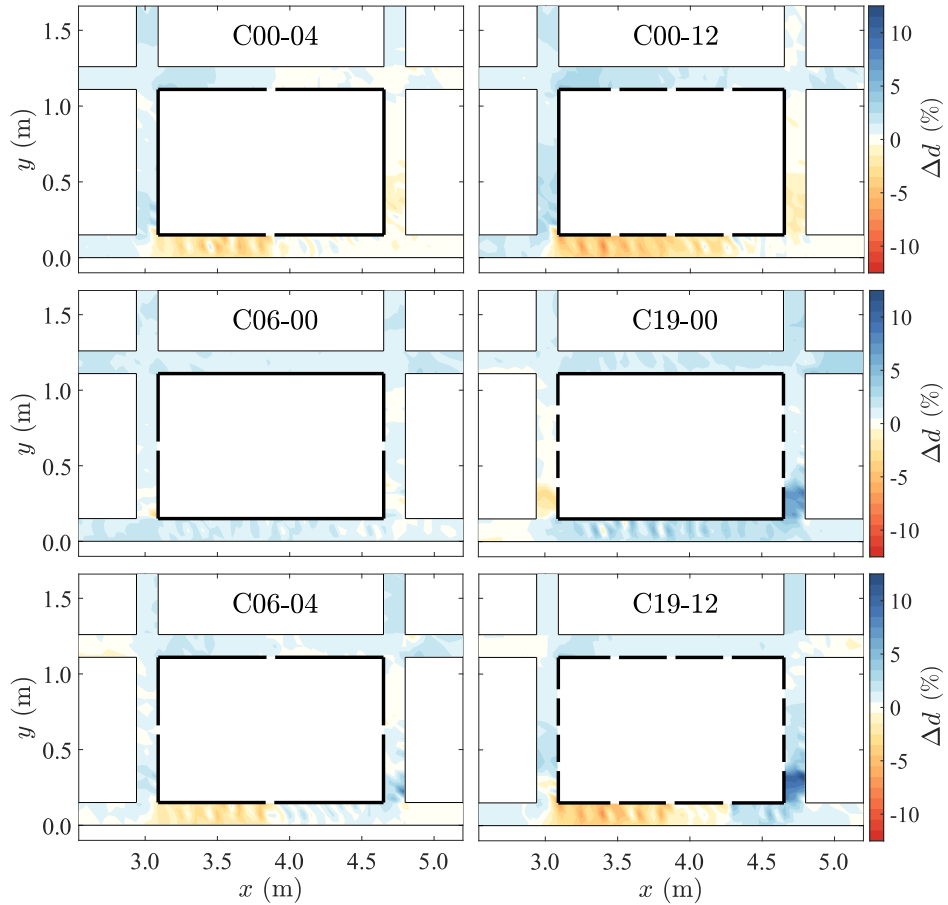


Figure 4: Relative difference in flow depth, Δd (Eq. 6), in the streets, with respect to the reference case C00-00. Cool colors indicate areas where flow depths are greater than in the reference case, while warm colours indicate areas where flow depths are smaller.

353 *3.2. Discharges and bulk-velocity in the streets*

354 Figure 5 shows an overview of the discharges in the streets and urban
355 block for all cases. The inlet and outlet discharges (monitored by electro-
356 magnetic flowmeters) are indicated by shaded boxes; the discharges com-
357 puted using Equation (1) or (2) are highlighted in purple and blue colours,
358 depending on the considered extrapolation method, detailed in Appendix C
359 (no-slip condition or an average between slip and no-slip conditions); and the
360 discharges computed from the mass conservation equation are highlighted in
361 orange colour. In the middle of the block, the intrusion discharge is high-
362 lighted in pink, obtained as the average between the sum of discharges en-
363 tering (green arrows) and leaving (red arrows) the block along with the cor-
364 responding uncertainty that includes the errors coming from the measuring
365 instruments (electromagnetic flowmeter and ADV) and from the discharge
366 computation method. The uncertainty was estimated as half the difference
367 between entering and leaving discharges. Due to additional ADV measure-
368 ments, several values can be obtained; the largest one is shown in Figure 5.
369 All the discharge values are shown as a percentage of the total inlet discharge
370 ($Q_{inT} = 6.5 \text{ ls}^{-1}$). In the streets, the direction of the flow is the same for all
371 cases, i.e. from upstream to downstream in the two longitudinal streets, and
372 from right to left in the two transverse streets. In contrast, the direction of
373 the exchange flow through the openings may vary from one case to another.

374 Regarding the discharge magnitude, when using case C00-00 as a reference
375 flow situation, Figure 5 shows that the change in porosity: i) significantly
376 affects the discharges in the streets surrounding the urban block; ii) signifi-
377 cantly affects the discharge entering the block, which logically increases with

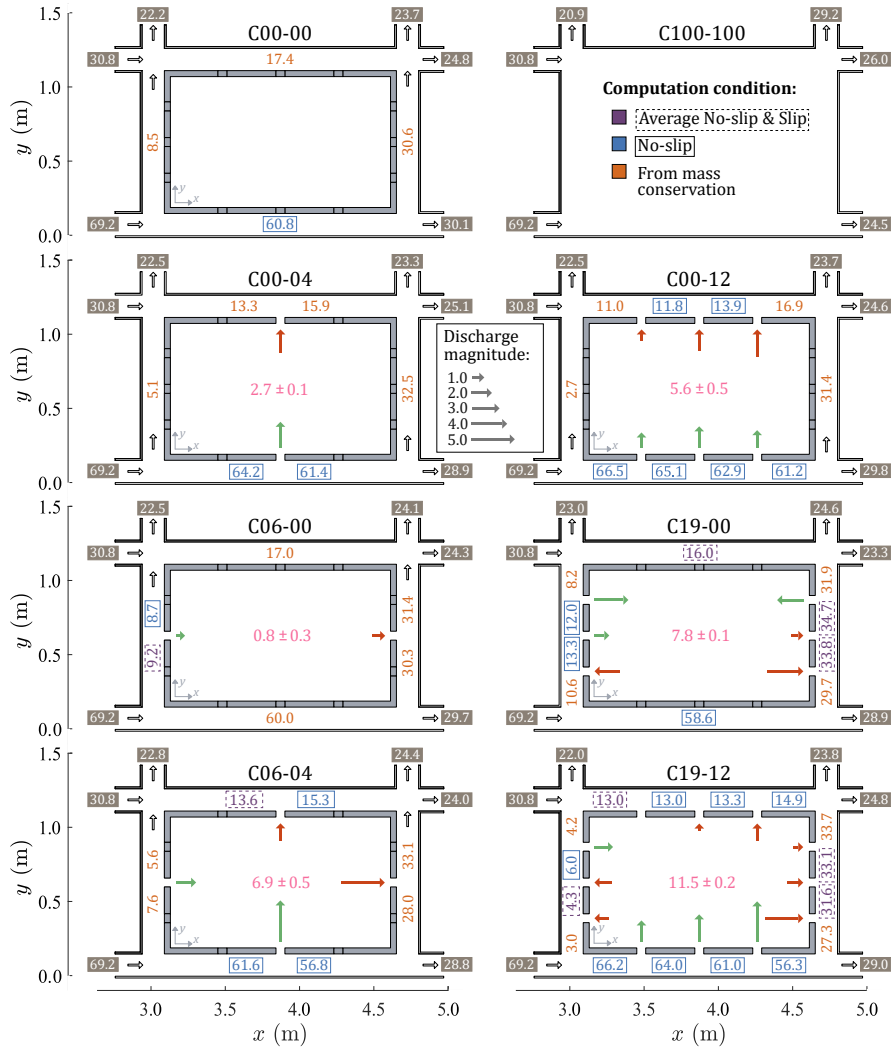


Figure 5: Discharges in the streets, urban block, and inlet and outlet discharges for all flow cases. All the discharge values are presented as a percentage of the total inlet discharge, $Q_{inT} = 6.5 \text{ l s}^{-1}$. The inlet and outlet discharges (measured with the electromagnetic flowmeters) are indicated by shaded boxes. The discharges computed from Eq. (1) or (2) are indicated by purple and blue boxes, depending on the boundary condition used to compute them, an average between slip and no-slip and no-slip, respectively. The discharges deduced from mass conservation are highlighted in orange colour. The intrusion discharge in the block and the associated uncertainty are highlighted in pink colour.

378 an increasing porosity; and iii) hardly alters the outlet discharges, putting
 379 aside the extreme case without block (C100-100).

380 The relative differences in discharge in the streets, ΔQ_{st} , with respect
 381 to the reference flow case, are shown in Figure 6. They are computed at
 382 the upstream end of the four surrounding streets. The relative difference
 383 ΔQ_{st} increases with block porosity, for instance, for cases C00-04 and C00-
 384 12, $\Delta Q_{st} = -40\%$ and -70% , in the upstream street, $\Delta Q_{st} = -24\%$ and -36%
 385 in the left street, and $\Delta Q_{st} = 6\%$ to 10% in the right street, respectively.
 386 The same tendency is observed when comparing cases C06-00 and C19-00,
 387 or cases C06-04 and C19-12.

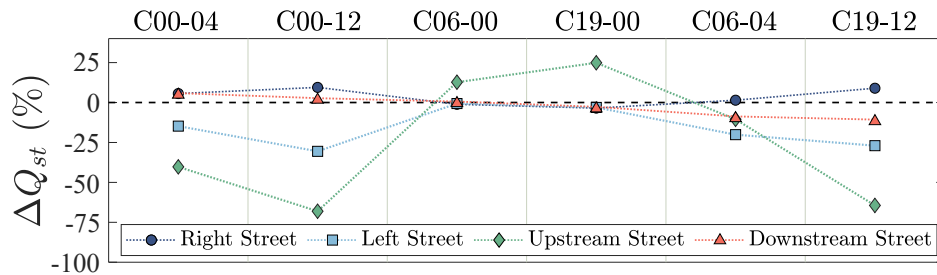


Figure 6: Relative difference in discharge with respect to the reference case, ΔQ_{st} , at the upstream end of each street surrounding the urban block (i.e. at $x = 3.09$ m for the right and left streets and at $y = 0.15$ m for the upstream and downstream streets).

388 The exchange discharges through the block openings also increase with
 389 the porosity (see Figure 7). However, no tendency arises for the intrusion
 390 discharge as a function of the porosity. For instance, if we compare 3 pairs
 391 of cases where the porosity is increased by 200%, the increase in discharge is
 392 107% from C00-04 to C00-12, 830% from C06-00 to C19-00 and 70% from
 393 C06-04 to C19-12.

394 It is also interesting to investigate the influence of the porosity distri-

395 bution for a fixed total number of openings along the block walls. For two
396 openings (cases C00-04 and C06-00), Figure 7 indicates that the discharge
397 through the urban block is greater, by approximately 240%, with openings in
398 the right and left walls than with openings in the upstream and downstream
399 walls. The same result holds for 6 openings, when comparing cases C00-12
400 and C19-00, with a higher exchange discharge of 40% when the openings are
401 located in the left and right streets. Hence, the exchange discharge between
402 streets and block does not depend only on the porosity value. This is a more
403 complex process, depending on the location of the openings, the flow orienta-
404 tion through these openings, the flow circulation within the block, and flow
405 depths and discharges in the surrounding streets.

406 Finally, when moving away from the block, the outlet discharges are
407 hardly affected by a change in porosity, the flow distribution among the four
408 outlets is rather constant from one case to another, when putting aside the
409 extreme case without block (C100-100), as shown at the top right of Figure 5.
410 The maximum variation with respect to the reference case remains limited to
411 around 2%. To verify whether this was due to the imposed weir heights, ad-
412 ditional experiments were conducted (for detailed information see Appendix
413 D), by changing the hydraulic boundary conditions (inflow discharge distri-
414 bution between left and right streets, and the height of the weirs) and the
415 longitudinal and transverse slopes. The results obtained are similar as in the
416 main experiment: the urban block porosity does not significantly impact the
417 discharge distribution among the four outlets. The latter is mainly driven
418 by the presence of the urban block, irrespective of the porosity value of its
419 walls.

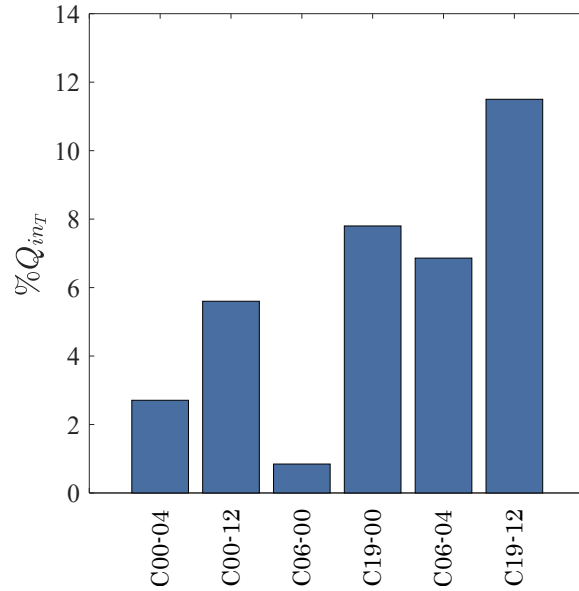


Figure 7: Flow rate through the urban block for six flow cases, as a percentage of the total inflow discharge, $Q_{inT} = 6.5 \text{ l s}^{-1}$.

420 The bulk velocities in the streets for the six cases with a porous block
 421 are now compared with those of the reference case. Figure 8 shows the rel-
 422 ative difference in bulk velocity (ΔU_{x_b} and ΔU_{y_b} , as appropriate) for all the
 423 streets. In the streets surrounding the block, the bulk velocities considerably
 424 vary with respect to the reference case, and this variation increases with
 425 an increasing porosity. Among the six cases presented in the figure, for all
 426 the streets, the larger velocity difference from the reference case corresponds
 427 to cases with greater porosity, i.e. cases C00-12, C19-00 and C19-12. The
 428 biggest differences are observed in the upstream street, with maximum dif-
 429 ferences between 65 and 70% for cases C00-12, C19-00 and C19-12. As the
 430 variation in flow depth in the streets with respect to the reference case is
 431 limited (Section 3.1), the significant variation in velocity observed here is

432 mainly due to the variation in discharge in the streets.

433 *3.3. Surface velocity and recirculation flow patterns*

434 Figure 9 shows the spatial distribution of the time-averaged surface veloc-
435 ity magnitude, U_s , along with the time-averaged streamlines, in all accessible
436 areas. For all cases, the surface velocity magnitude ranges from 0 to about
437 60 cm s^{-1} ($0.0 - 1.9 \text{ m s}^{-1}$ at the prototype scale). The highest velocity mag-
438 nitude is observed in the right street due to the high inflow discharge at the
439 entrance of this street. The velocity in the left street is three to four times
440 lower. The upstream street exhibits one or two recirculating flow areas (de-
441 pending on the flow case) induced by the shearing with the flow in the right
442 street, and on average, the flow along this street is the slowest among all the
443 streets. The downstream street is characterized by a wide range of velocity
444 magnitude (from 0 to 50 cm s^{-1}), with the highest velocities mainly located
445 along the right wall, opposite to the block under study. Besides, the velocity
446 magnitude within the urban block is significantly smaller than in the streets,
447 about 20 cm s^{-1} maximum (0.63 m s^{-1} at the real-world prototype scale), a
448 third of the maximum velocity on the streets.

449 Within the urban block, from two to five recirculating flow areas can be
450 observed. The spatial distribution and the size of the recirculating flow cells
451 are mainly driven by the direction of the jets through the openings. For in-
452 stance, case C00-04 shows two cells, nearly symmetrical, on each side of the
453 entering jet. In contrast, case C06-00 (with the same number of openings but
454 aligned with the longitudinal direction) shows a main recirculating flow cell
455 and a smaller secondary one on the right side upstream. These results are in
456 agreement with those presented in several studies on shallow reservoirs (e.g.

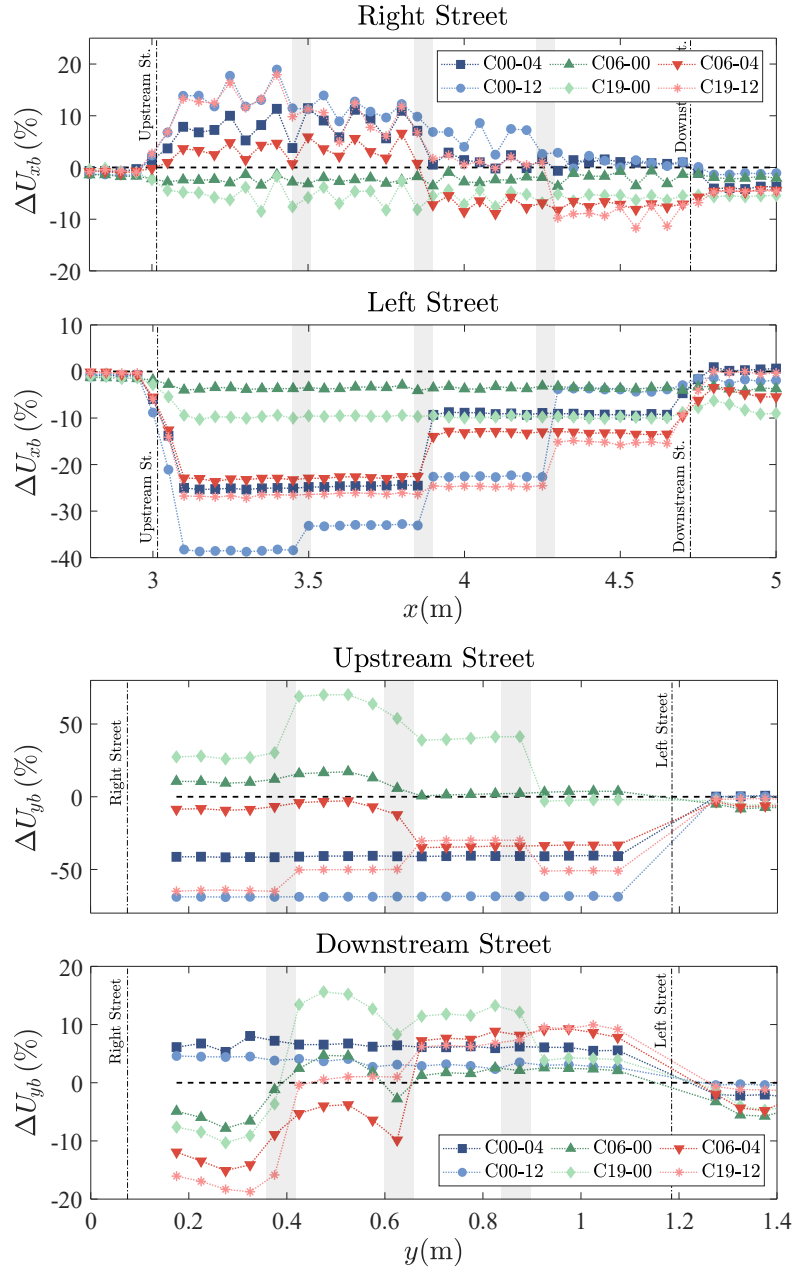


Figure 8: Relative difference in bulk velocity with respect to the reference case, ΔU_{xb} and ΔU_{yb} , in the longitudinal direction (x -axis) and transverse direction (y -axis), respectively. Vertical shaded bands indicate the location of the openings along the urban block walls.

457 Dewals et al., 2008; Dufresne et al., 2010; Goltsman and Saushin, 2019). The
458 difference in the flow pattern between C00-04 and C06-00 is partly due to the
459 length-width ratio of the reservoir, which is higher for C06-00, and to the ex-
460 change flow rate magnitude (three times higher for C00-04). A similar trend
461 is observed for cases C00-12 and C19-00, with the same number of openings,
462 but along opposite axes: case C00-12 exhibits two main recirculation cells
463 (one larger than the other), plus three small recirculation cells driven by
464 the jets through the right wall; however, C19-00, exhibits a single recircula-
465 tion cell and three much smaller ones, two upstream and one downstream.
466 Finally, case C06-04 comprises two main recirculation cells and a small one
467 upstream, while case C19-12 comprises two main recirculation cells and three
468 small ones next to the right wall. As expected the higher number of openings
469 increases the number of recirculation cells. We can thus conclude that the
470 flow pattern inside the urban block depends on its length-width ratio (length
471 = main jet direction), the magnitude of the jets, the number of openings
472 (porosity value) and their locations (porosity distribution).

473 In absence of urban block (case C100-100), two recirculating flow cells of
474 similar size are generated. Contrary to what is observed within the block,
475 here the flow velocity in the recirculation cells does not decrease as drastically
476 compared to the streets velocity, mainly in the downstream cell. Amongst
477 all cases, here is where the highest average velocities are found.

478 **4. Flood risk to pedestrians**

479 Assuming that the surface velocity (calculated with LSPIV) is equal to
480 the depth-averaged velocity (valid assumption according to figures shown

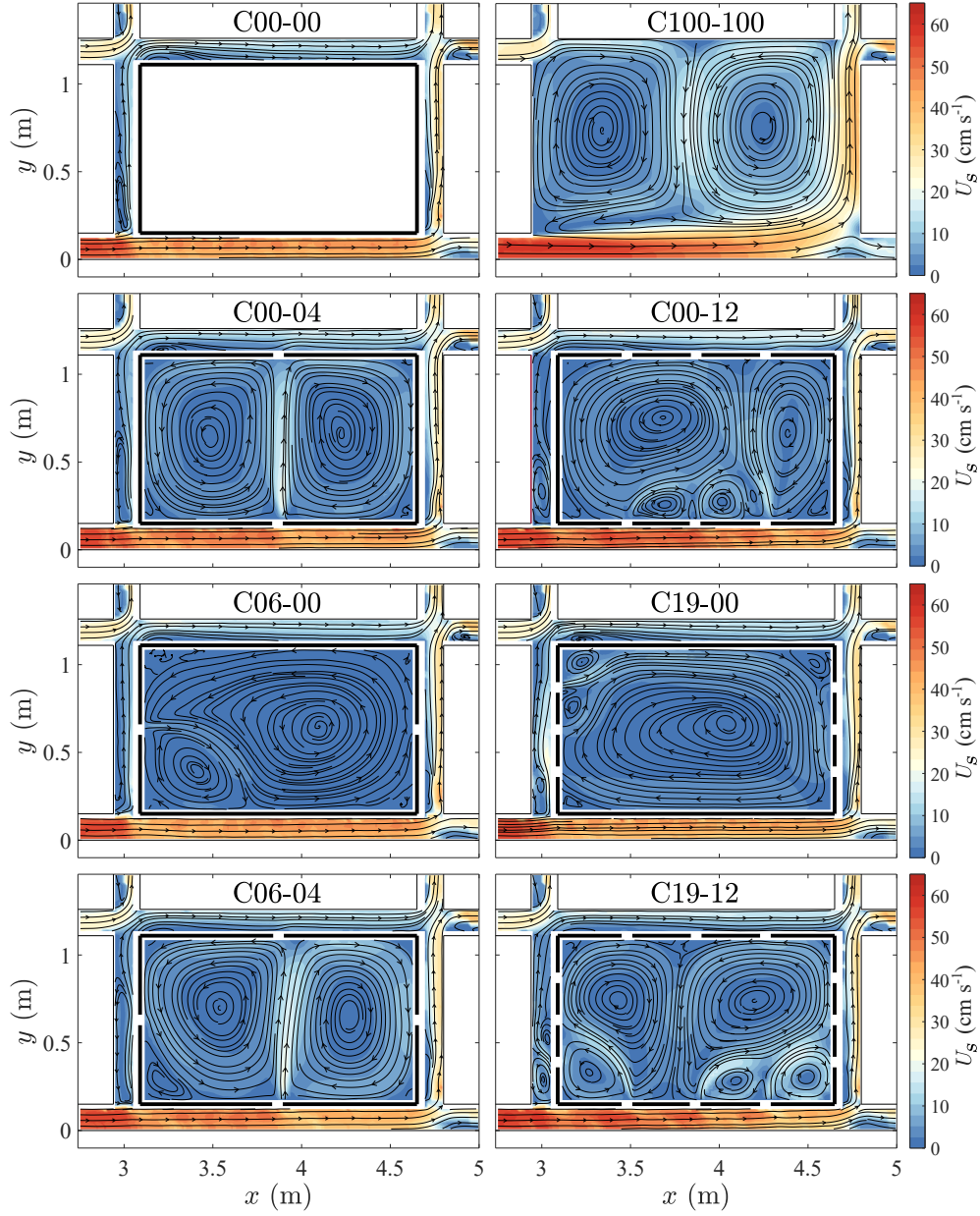


Figure 9: Time-averaged surface velocity magnitude, U_s , and streamlines in the streets and within the urban block (derived from LSPIV data).

481 in the Appendix B), using the spatial distribution of local flow depth and
482 applying the Froude similarity detailed in Eqs. (4) and (5), a 2-D map of
483 flood risk level for pedestrians was built for each flow case (Figure 10). This
484 enables to assess the impact of the urban block porosity on the risk level.
485 The latter is defined by the criteria proposed in Figure 2.

486 For each flow case, the flood risk ranges from *low* to *high*, the highest
487 risk being located in the right street due to the high velocity and flow depth
488 along this street. The risk level is also important in the downstream street
489 near the right sidewalk, with strong flow velocities (even in absence of block,
490 as it is the main path of the high-speed stream as previously mentioned). In
491 contrast, the level of risk inside the block is small due to the very low velocity
492 in this open area.

493 Figure 10 also shows that block porosity can enhance flood risk level at one
494 specific location while reducing it at another. For instance, when comparing
495 C00-12 with C00-00, the risk decreases in the upstream street but increases
496 in the right street. This same tendency is observed in these streets, to a
497 greater or lesser extent, for the other cases, except for case C19-00, where a
498 local increase in the level of risk is predicted in the vicinity of the openings in
499 the upstream street. For the other streets, only limited and local differences
500 in the level of risk are predicted, mainly in the vicinity of the openings, as
501 for instance, in the downstream street of case C19-12, whit a higher level of
502 risk. Within the urban block, the modifications of the level of risk are mainly
503 due to changes in velocity, since flow depths are almost the same throughout
504 the area for all cases. The areas of greatest risk occur near the openings
505 along the incoming flow jets. Therefore, the impact of porosity on the flood

506 risk increases when porosity increases, but this is spatially limited to to the
507 vicinity of the openings.

508 **5. Conclusions**

509 Urban flood flows were experimentally investigated on a 5.4 m long and
510 3.2 m wide physical model, representing a rectangular urban block and four
511 adjacent streets. The focus of the study was on assessing the effects of the
512 porosity of the urban block walls (openings such as gates, windows and doors)
513 on the spatial distribution of flow depth and velocity in a street network of
514 limited spatial extent. The effect of the block porosity on the flood risk to
515 pedestrians was also estimated.

516 Eight flow cases have been studied: a reference case with a non-porous
517 urban block; six cases varying the porosity value and the spatial distribution
518 of the porosity along the block walls; and an extreme case without block. For
519 each case, the flow depth and surface velocity were measured in the streets
520 and within the block. The discharge in each street reach and the exchange
521 discharges between block and streets were also measured.

522 Block porosity was found to have a small influence on the spatial dis-
523 tribution of flow depths. In the streets surrounding the block, the average
524 difference in flow depth (compared to the reference case) is approximately
525 of 1.5%, and the maximum difference of 12%. When moving away from the
526 block, these two percentages fall at 1% and 3%, respectively. It should be
527 noted that the flow depth can strongly vary from either side of a block wall,
528 i.e. between the block and the street: from -14% (smaller flow depth in the
529 street) to +10% (higher flow depth in the street). This result questions the

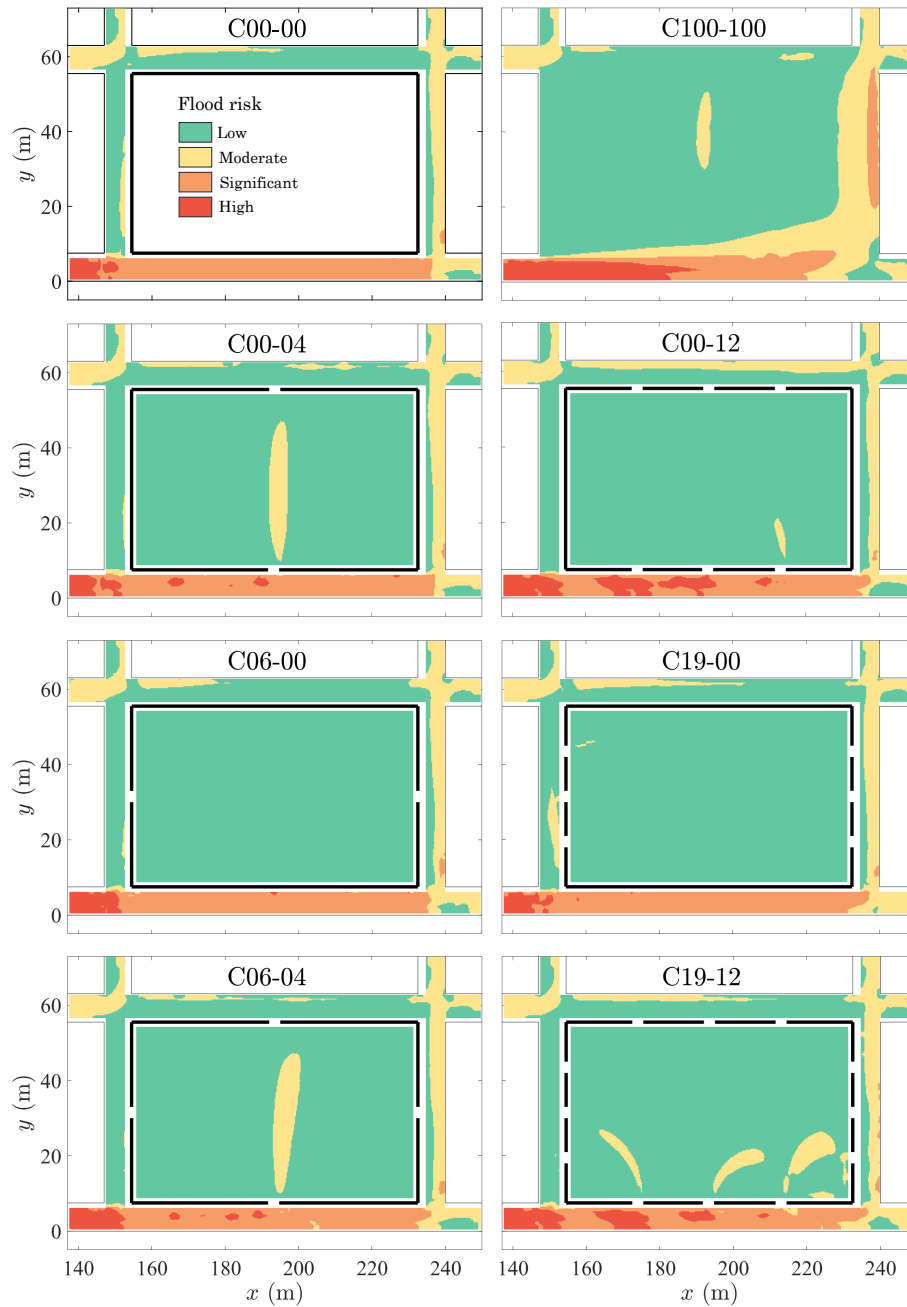


Figure 10: Flood risk maps for adult pedestrians, for each flow case, obtained by scaling flow depths and velocities at the real-world prototype scale using Froude similarity (Eqs. 4 and 5), and with $\lambda_z = 10$.

530 common practices to consider the flow level in the building equal to that in
531 the adjacent street to estimate the potential damages of a flooding scenario.

532 The impact of the block porosity is far more significant on the local bulk
533 velocity and discharges in the streets surrounding the block (changes in flow
534 discharge up to 70% compared with the reference case). Inside the block,
535 the value and distribution of the porosity have a significant influence on the
536 flow pattern. The number and size of the recirculating flow cells are mainly
537 driven by the magnitude and locations of the exchange inflows and outflows
538 between street and block. However, when moving further away from the
539 block, the influence of the porosity is limited, similar to that observed for
540 flow depths, and could therefore be neglected.

541 Last, the variation of block porosity was found to modify the flood risk
542 to pedestrians only locally near the openings, both in the street and block.
543 As a result, if assessing the flood risk at the scale of a building entrance (one
544 address) is required, it is recommended to take into account the porosity of
545 the buildings and urban blocks when performing risk maps. When assessing
546 the risk at a more global scale, present results seem to indicate a limited
547 impact of the porosity; still this result will have to be confirmed by further
548 studies.

549 **6. Acknowledgements**

550 The authors acknowledge the financial support offered by the French Na-
551 tional Research Agency (ANR) for the project DEUFI (under grant ANR-
552 18-CE01-0020).

553 **References**

554 Abt, S., Wittier, R., Taylor, A., Love, D., 1989. HUMAN STABILITY
555 IN A HIGH FLOOD HAZARD ZONE. *Journal of the American Wa-*
556 *ter Resources Association* 25, 881–890. doi:10.1111/j.1752-1688.1989.
557 *tb05404.x*.

558 Araud, Q., Finaud-Guyot, P., Lawniczak, F., François, P., Vazquez, J., Mosé,
559 R., 2014. Modeling Flood in an Urban Area: Validation of Numerical Tools
560 Against Experimental Data, in: Gourbesville, P., Cunge, J., Caignaert, G.
561 (Eds.), *Advances in Hydroinformatics: SIMHYDRO 2012 – New Frontiers*
562 *of Simulation*. Springer Singapore, Singapore, pp. 207–220. doi:10.1007/
563 *978-981-4451-42-0_18*.

564 Arrighi, C., Oumeraci, H., Castelli, F., 2017. Hydrodynamics of pedestrians'
565 instability in floodwaters. *Hydrology and Earth System Sciences* 21, 515–
566 531. doi:10.5194/hess-21-515-2017.

567 Arrighi, C., Pregnolato, M., Dawson, R., Castelli, F., 2019. Preparedness
568 against mobility disruption by floods. *Science of The Total Environment*
569 654, 1010 – 1022. doi:https://doi.org/10.1016/j.scitotenv.2018.
570 11.191.

571 Bazin, P.H., Mignot, E., Paquier, A., 2017. Computing flooding of crossroads
572 with obstacles using a 2d numerical model. *Journal of Hydraulic Research*
573 55, 72–84. doi:10.1080/00221686.2016.1217947.

574 Chanson, H., 2004. *Hydraulics of open channel flow*. Elsevier.

- 575 Chanson, H., Brown, R., McIntosh, D., 2014. Human body stability in
576 floodwaters: The 2011 flood in brisbane cbd, in: Chanson, H., Toombes,
577 L. (Eds.), Hydraulic Structures and Society - Engineering Challenges and
578 Extremes: Proceedings of the 5th IAHR International Symposium on Hy-
579 draulic Structures (ISHS2014), The University of Queensland, Australia.
580 pp. 1–9. doi:10.14264/uql.2014.48.
- 581 Chen, W., Wang, X., Deng, S., Liu, C., Xie, H., Zhu, Y., 2019. Integrated
582 urban flood vulnerability assessment using local spatial dependence-based
583 probabilistic approach. *Journal of Hydrology* 575, 454 – 469. doi:<https://doi.org/10.1016/j.jhydro1.2019.05.043>.
584
- 585 Costabile, P., Costanzo, C., Lorenzo], G.D., Macchione, F., 2020. Is local
586 flood hazard assessment in urban areas significantly influenced by the phys-
587 ical complexity of the hydrodynamic inundation model? *Journal of Hy-*
588 *drology* 580, 124231. doi:[https://doi.org/10.1016/j.jhydro1.2019.](https://doi.org/10.1016/j.jhydro1.2019.124231)
589 [124231](https://doi.org/10.1016/j.jhydro1.2019.124231).
- 590 Cox, R., Shand, T., Blacka, M., 2010. Australian rainfall and runoff revision
591 project 10: appropriate safety criteria for people. *Water Research* 978,
592 085825–9454.
- 593 Dewals, B., Kantoush, S., Erpicum, S., Piroton, M., Schleiss, A., 2008.
594 Experimental and numerical analysis of flow instabilities in rectangular
595 shallow basins. *Environmental Fluid Mechanics* 8, 31–54. doi:10.1007/
596 s10652-008-9053-z.
- 597 Dufresne, M., Dewals, B.J., Erpicum, S., Archambeau, P., Piroton, M.,

- 598 2010. Classification of flow patterns in rectangular shallow reservoirs. *Journal of Hydraulic Research* 48, 197–204. doi:10.1080/00221681003704236.
- 599
- 600 El Kadi Abderrezzak, K., Paquier, A., Mignot, E., 2009. Modelling flash
601 flood propagation in urban areas using a two-dimensional numerical model.
602 *Natural Hazards* 50, 433–460. doi:10.1007/s11069-008-9300-0.
- 603 Finaud-Guyot, P., Garambois, P.A., Araud, Q., Lawniczak, F., François, P.,
604 Vazquez, J., Mosé, R., 2018. Experimental insight for flood flow repartition
605 in urban areas. *Urban Water Journal* 15, 242–250. doi:10.1080/1573062X.
606 2018.1433861.
- 607 Finaud-Guyot, P., Garambois, P.A., Dellinger, G., Lawniczak, F., François,
608 P., 2019. Experimental characterization of various scale hydraulic sig-
609 natures in a flooded branched street network. *Urban Water Journal* 16,
610 609–624. doi:10.1080/1573062X.2020.1713173.
- 611 Foster, D., Cox, R., 1973. Stability of children on roads used as floodways.
612 University of New South Wales Water Research Laboratory technical re-
613 port 73, 13.
- 614 Fujita, I., Muste, M., Kruger, A., 1998. Large-scale particle image velocime-
615 try for flow analysis in hydraulic engineering applications. *Journal of Hy-
616 draulic Research* 36, 397–414. doi:10.1080/00221689809498626.
- 617 Galuppini, G., Quintilliani, C., Arosio, M., Barbero, G., Ghilardi, P., Ma-
618 nenti, S., Petaccia, G., Todeschini, S., Ciaponi, C., Martina, M.L.V.,
619 Creaco, E., 2020. A unified framework for the assessment of multiple

- 620 source urban flash flood hazard: the case study of monza, italy. *Urban*
621 *Water Journal* 17, 65–77. doi:10.1080/1573062X.2020.1734950.
- 622 Gómez, M., Martínez, E., Russo, B., 2018. Experimental and Numerical
623 Study of Stability of Vehicles Exposed to Flooding, in: Gourbesville, P.,
624 Cunge, J., Caignaert, G. (Eds.), *Advances in Hydroinformatics*, Springer
625 Singapore, Singapore. pp. 595–605. doi:10.1007/978-981-10-7218-5_42.
- 626 Goltsman, A., Saushin, I., 2019. Flow pattern of double-cavity flow at high
627 reynolds number. *Physics of Fluids* 31, 065101. doi:10.1063/1.5099702.
- 628 Goring, D.G., Nikora, V.I., 2002. Despiking acoustic doppler velocimeter
629 data. *Journal of Hydraulic Engineering* 128, 117–126. doi:10.1061/(ASCE)
630 0733-9429(2002)128:1(117).
- 631 Guinot, V., 2012. Multiple porosity shallow water models for macroscopic
632 modelling of urban floods. *Advances in Water Resources* 37, 40 – 72.
633 doi:https://doi.org/10.1016/j.advwatres.2011.11.002.
- 634 Heller, V., 2011. Scale effects in physical hydraulic engineering models.
635 *Journal of Hydraulic Research* 49, 293–306. doi:10.1080/00221686.2011.
636 578914.
- 637 Ishigaki, T., 2003. Hydraulic model tests of inundation in urban area with
638 underground space, in: *Proc. of 30th IAHR Congress, Greece, 2003*, pp.
639 487–493.
- 640 Ishigaki, T., Kawanaka, R., Onishi, Y., Shimada, H., Toda, K., Baba, Y.,
641 2009. Assessment of Safety on Evacuating Route During Underground

642 Flooding, in: *Advances in Water Resources and Hydraulic Engineering*.
643 Springer Berlin Heidelberg, Berlin, Heidelberg, pp. 141–146. doi:10.1007/
644 978-3-540-89465-0_27.

645 Jakob, M., Stein, D., Ulmi, M., 2012. Vulnerability of buildings to debris flow
646 impact. *Natural Hazards* 60, 241–261. doi:10.1007/s11069-011-0007-2.

647 Jonkman, S., Penning-Rowsell, E., 2008. Human Instability in Flood Flows
648 ¹. *JAWRA Journal of the American Water Resources Association* 44,
649 1208–1218. doi:10.1111/j.1752-1688.2008.00217.x.

650 Kantoush, S.A., Schleiss, A.J., Sumi, T., Murasaki, M., 2011. Lspiv im-
651 plementation for environmental flow in various laboratory and field cases.
652 *Journal of Hydro-environment Research* 5, 263 – 276. doi:https://doi.
653 org/10.1016/j.jher.2011.07.002.

654 Karvonen, T., Hepojoki, A., Kotala, J., Huhta, H.K., 2000. The use of
655 physical models in dam-break flood analysis, RESCDAM. Final report of
656 Helsinki University of Technology. Technical Report. Helsinki.

657 Kramer, M., Terheiden, K., Wieprecht, S., 2016. Safety criteria for the
658 trafficability of inundated roads in urban floodings. *International Journal*
659 *of Disaster Risk Reduction* 17, 77–84. doi:10.1016/j.ijdrr.2016.04.
660 003.

661 Lo, W.C., Tsao, T.C., Hsu, C.H., 2012. Building vulnerability to debris
662 flows in Taiwan: a preliminary study. *Natural Hazards* 64, 2107–2128.
663 doi:10.1007/s11069-012-0124-6.

- 664 Macchione, F., Costabile, P., Costanzo, C., Lorenzo, G.D., 2019. Extracting
665 quantitative data from non-conventional information for the hydraulic re-
666 construction of past urban flood events. a case study. *Journal of Hydrology*
667 576, 443 – 465. doi:<https://doi.org/10.1016/j.jhydro1.2019.06.031>.
- 668 Maiwald, H., Schwarz, J., 2012. Damage and loss prediction model consid-
669 ering inundation level, flow velocity and vulnerability of building types,
670 Dubrovnik, Croatia. pp. 53–65. doi:10.2495/FRIAR120051.
- 671 Martínez-Gomariz, E., Gómez, M., Russo, B., 2016. Experimental study of
672 the stability of pedestrians exposed to urban pluvial flooding. *Natural*
673 *Hazards* 82, 1259–1278. doi:10.1007/s11069-016-2242-z.
- 674 Martínez-Gomariz, E., Gómez, M., Russo, B., Djordjević, S., 2017. A new
675 experiments-based methodology to define the stability threshold for any
676 vehicle exposed to flooding. *Urban Water Journal* 14, 930–939. doi:10.
677 1080/1573062X.2017.1301501. publisher: Taylor & Francis.
- 678 Meselhe, E.A., Peeva, T., Muste, M., 2004. Large scale particle image ve-
679 locimetry for low velocity and shallow water flows. *Journal of Hydraulic*
680 *Engineering* 130, 937–940. doi:10.1061/(ASCE)0733-9429(2004)130:
681 9(937).
- 682 Mignot, E., Paquier, A., Ishigaki, T., 2006. Comparison of numerical and
683 experimental simulations of a flood in a dense urban area. *Water Science*
684 *and Technology* 54, 65–73. doi:10.2166/wst.2006.596.
- 685 Milanesi, L., Pilotti, M., Bacchi, B., 2016. Using web-based observations

686 to identify thresholds of a person's stability in a flow. *Water Resources*
687 *Research* 52, 7793–7805. doi:10.1002/2016WR019182.

688 Milanesi, L., Pilotti, M., Belleri, A., Marini, A., Fuchs, S., 2018. Vulnerability
689 to flash floods: A simplified structural model for masonry buildings. *Water*
690 *Resources Research* 54, 7177–7197. doi:10.1029/2018WR022577.

691 Milanesi, L., Pilotti, M., Ranzi, R., . A conceptual model of people's vul-
692 nerability to floods. *Water Resources Research* 51, 182–197. doi:10.1002/
693 2014WR016172.

694 de Moel, H., van Alphen, J., Aerts, J.C.J.H., 2009. Flood maps in europe—
695 methods, availability and use. *Natural Hazards and Earth System Sciences*
696 9, 289–301. doi:10.5194/nhess-9-289-2009.

697 Muste, M., Xiong, Z., Bradley, A., Kruger, A., 2000. Large-scale parti-
698 cle image velocimetry—a reliable tool for physical modeling, in: *Building*
699 *Partnerships*, pp. 1–10. doi:10.1061/40517(2000)311.

700 Paquier, A., Bazin, P.H., Abderrezzak, K.E.K., 2019. Sensitivity of 2d hy-
701 drodynamic modelling of urban floods to the forcing inputs: lessons from
702 two field cases. *Urban Water Journal* 0, 1–10. doi:10.1080/1573062X.
703 2019.1669200.

704 Rapp, B.E., 2017. Chapter 9 - fluids, in: Rapp, B.E. (Ed.), *Microflu-*
705 *idics: Modelling, Mechanics and Mathematics*. Elsevier, Oxford. *Micro*
706 *and Nano Technologies*, pp. 243 – 263. doi:https://doi.org/10.1016/
707 B978-1-4557-3141-1.50009-5.

- 708 Russo, B., Gómez, M., Macchione, F., 2013. Pedestrian hazard criteria
709 for flooded urban areas. *Natural Hazards* 69, 251–265. doi:10.1007/
710 s11069-013-0702-2.
- 711 Shu, C., Xia, J., Falconer, R.A., Lin, B., 2011. Incipient velocity for partially
712 submerged vehicles in floodwaters. *Journal of Hydraulic Research* 49, 709–
713 717. doi:10.1080/00221686.2011.616318.
- 714 Soares-Frazão, S., Lhomme, J., Guinot, V., Zech, Y., 2008. Two-dimensional
715 shallow-water model with porosity for urban flood modelling. *Journal of*
716 *Hydraulic Research* 46, 45–64. doi:10.1080/00221686.2008.9521842.
- 717 Sturm, M., Gems, B., Keller, F., Mazzorana, B., Fuchs, S., Papathoma-
718 Köhle, M., Aufleger, M., 2018. Experimental analyses of impact forces on
719 buildings exposed to fluvial hazards. *Journal of Hydrology* 565, 1 – 13.
720 doi:<https://doi.org/10.1016/j.jhydro1.2018.07.070>.
- 721 Takahashi, S., Endoh, K., Muro, Z., 1992. Experimental study on people's
722 safety against overtopping waves on breakwaters. *Report on the Port and*
723 *Harbour Institute* 34, 4–31.
- 724 Teo, F.Y., Xia, J., Falconer, R.A., Lin, B., 2012. Experimental studies on
725 the interaction between vehicles and floodplain flows. *International Journal*
726 *of River Basin Management* 10, 149–160. doi:10.1080/15715124.2012.
727 674040. publisher: Taylor & Francis.
- 728 UNISDR, C., et al., 2015. *The human cost of natural disasters: A global*
729 *perspective* .

- 730 United Nations, Department of Economic and Social Affairs, Population Di-
731 vision, 2019. World urbanization prospects: The 2018 Revision. United
732 Nations, New York.
- 733 Xia, J., Falconer, R.A., Wang, Y., Xiao, X., 2014a. New criterion for the
734 stability of a human body in floodwaters. *Journal of Hydraulic Research*
735 52, 93–104. doi:10.1080/00221686.2013.875073.
- 736 Xia, J., Falconer, R.A., Xiao, X., Wang, Y., 2014b. Criterion of vehicle
737 stability in floodwaters based on theoretical and experimental studies. *Nat*
738 *Hazards* 70, 1619–1630. doi:10.1007/s11069-013-0889-2.
- 739 Xia, J., Teo, F.Y., Lin, B., Falconer, R.A., 2011. Formula of incipi-
740 ent velocity for flooded vehicles. *Nat Hazards* 58, 1–14. doi:10.1007/
741 s11069-010-9639-x.
- 742 Zhou, Q., Yu, W., Chen, A.S., Jiang, C., Fu, G., 2016. Experimental assess-
743 ment of building blockage effects in a simplified urban district. *Procedia*
744 *Engineering* 154, 844 – 852. doi:[https://doi.org/10.1016/j.proeng.](https://doi.org/10.1016/j.proeng.2016.07.448)
745 2016.07.448. 12th International Conference on Hydroinformatics (HIC
746 2016) - Smart Water for the Future.

747 **Appendix A. Time convergence of the flow depth and velocity**
748 **measurements**

749 *Appendix A.1. Flow depth*

750 The time convergence of the US signal was tested by performing 13 inde-
751 pendent flow depth measurements at various locations (in the streets, within
752 the block and in specific areas with significant fluctuations in flow depth,
753 such as crossroads). Each measurement was carried out for 400 s at a sam-
754 pling rate of 50 Hz. For each measurement, the time-averaged flow depth
755 over each partial acquisition duration was computed and compared to the
756 time-averaged flow depth over the total acquisition duration ($t = 400$ s), as:

$$\Delta d(n_{(t)}) = \frac{1}{n_{(t)}} \sum_{i=1}^{n_{(t)}} d_i - \frac{1}{n_{(t=400)}} \sum_{i=1}^{n_{(t=400)}} d_i \quad (\text{A.1})$$

757 where d_i is the instantaneous flow depth and $n_{(t)}$ is the number of samples
758 at time t . Then, the appropriate acquisition duration was defined as the
759 time, t , for which $\Delta d(n_{(t)})$ is lower than 0.3 mm (accuracy specified by the
760 manufacturer). As shown in Figure A.11, this duration was 50 s.

761 *Appendix A.2. ADV velocity data*

762 The time convergence of the ADV velocity data was tested by measur-
763 ing for 600 s at a sampling rate of 100 Hz. Although the ADV is capable
764 of measuring the three velocity components (u_x, u_y, u_z) , we focused on the
765 horizontal components (u_x, u_y) , which are used to compute the discharge in
766 the streets and also to be compared with the velocities obtained via LSPIV.
767 Velocity measurements were performed at 14 locations (eight in the streets

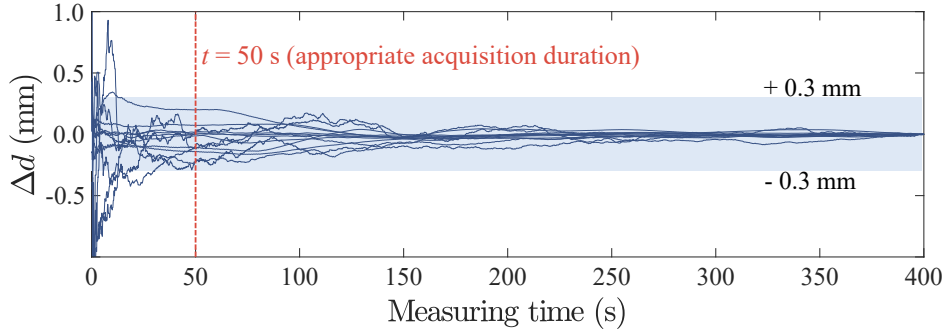


Figure A.11: Time convergence of the time-averaged flow depth at 13 various locations. Convergence is reached when $\Delta d \leq \pm 0.3$ mm (Eq. A.1) The shaded area indicates the probe accuracy (± 0.3 mm).

768 and six within the block) and for various cases (with the porous block, non-
 769 porous block and no block). We considered time convergence criterion of 3%,
 770 equal to the value of the standard error observed for the inlet discharge. The
 771 percentage error of the time-averaged velocity for each partial acquisition
 772 duration was obtained with the following expression:

$$\% \text{ Error}(n_{(t)}) = \frac{\frac{1}{n_{(t)}} \sum_{i=1}^{n_{(t)}} u_i - \frac{1}{n_{(t=600)}} \sum_{i=1}^{n_{(t=600)}} u_i}{\frac{1}{n_{(t=600)}} \sum_{i=1}^{n_{(t=600)}} u_i} \times 100 \quad (\text{A.2})$$

773 where u_i is the instantaneous velocity. In general, the convergence was ob-
 774 tained earlier in the streets (blue curves, Figure A.12) than within the block
 775 (red curves), therefore two appropriate acquisition durations were proposed,
 776 100 s for the ADV measurements within the streets and 200 s within the
 777 block.

778 *Appendix A.3. Surface velocity using LSPIV technique*

779 To evaluate the appropriate video recording duration for the LSPIV tech-
 780 nique, convergence tests were established by recording at a rate of 25 frames

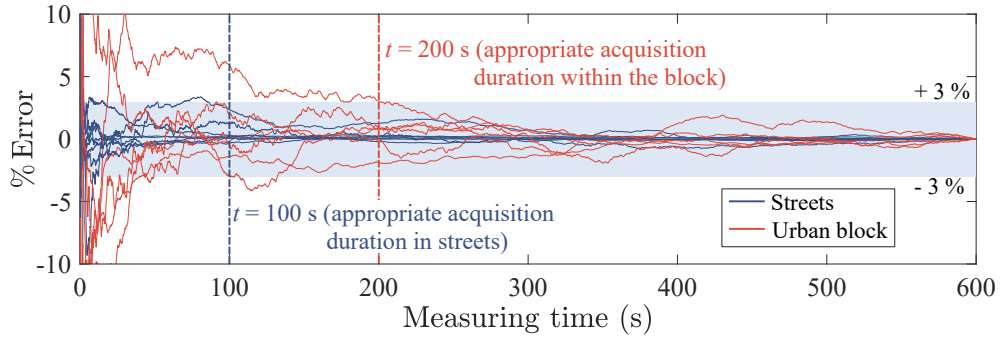


Figure A.12: Time convergence of the time-averaged streamwise velocity at 14 various locations. Convergence is reached when $\%Error \leq \pm 3\%$. The shaded area indicates the range $\pm 3\%$.

781 per second the velocity field of two cases (C19-12 and C100-100), with in-
 782 creasing durations (from 10 s to 180 s) and averaging in time the surface
 783 velocity over the entire area. The convergence criterion was the duration
 784 where the velocity difference for each point of the velocity field with respect
 785 to the velocity of the total recording time ($t = 180$ s) is equal or less than 1
 786 cm s^{-1} , for at least 80% of the total number of points in the measuring grid.
 787 The time-averaged velocity difference for each point in the velocity field was
 788 computed with the following expression:

$$|\Delta U_s(n(t))| = \left| \frac{1}{n(t)} \sum_{i=1}^{n(t)} u_i - \frac{1}{n(t=180)} \sum_{i=1}^{n(t=180)} u_i \right| \quad (\text{A.3})$$

789 The convergence was obtained earlier within the block, after 10 s (as
 790 indicated on the upper graph in Figure A.13) than in the streets, after 60
 791 s (lower graph in Figure A.13). For this reason it has been defined as the
 792 appropriate recording duration for the LSPIV technique, 60 s.

793 Additionally, figures A.14 and A.15 show the time-averaged surface ve-

794 locities for different recording durations, for cases C19-12 and C100-100,
 795 respectively. They provide a visual comparison of the velocity field over the
 796 entire domain, and it is possible to observe that globally the velocity field
 797 generally does not present important changes over time.

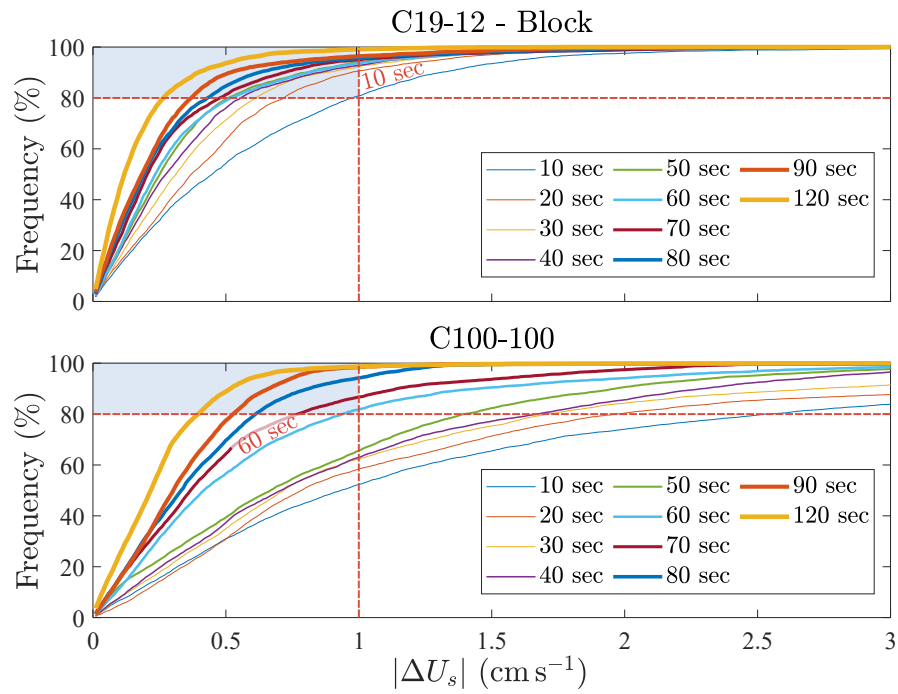


Figure A.13: Time convergence of the time-averaged surface velocity difference, ΔU_s , for various recording durations, from 10 s to 120 s, for cases C19-12 and C100-100. Convergence is reached when $|\Delta U_s| \leq 1 \text{ cm s}^{-1}$ and % Frequency $\geq 80\%$.

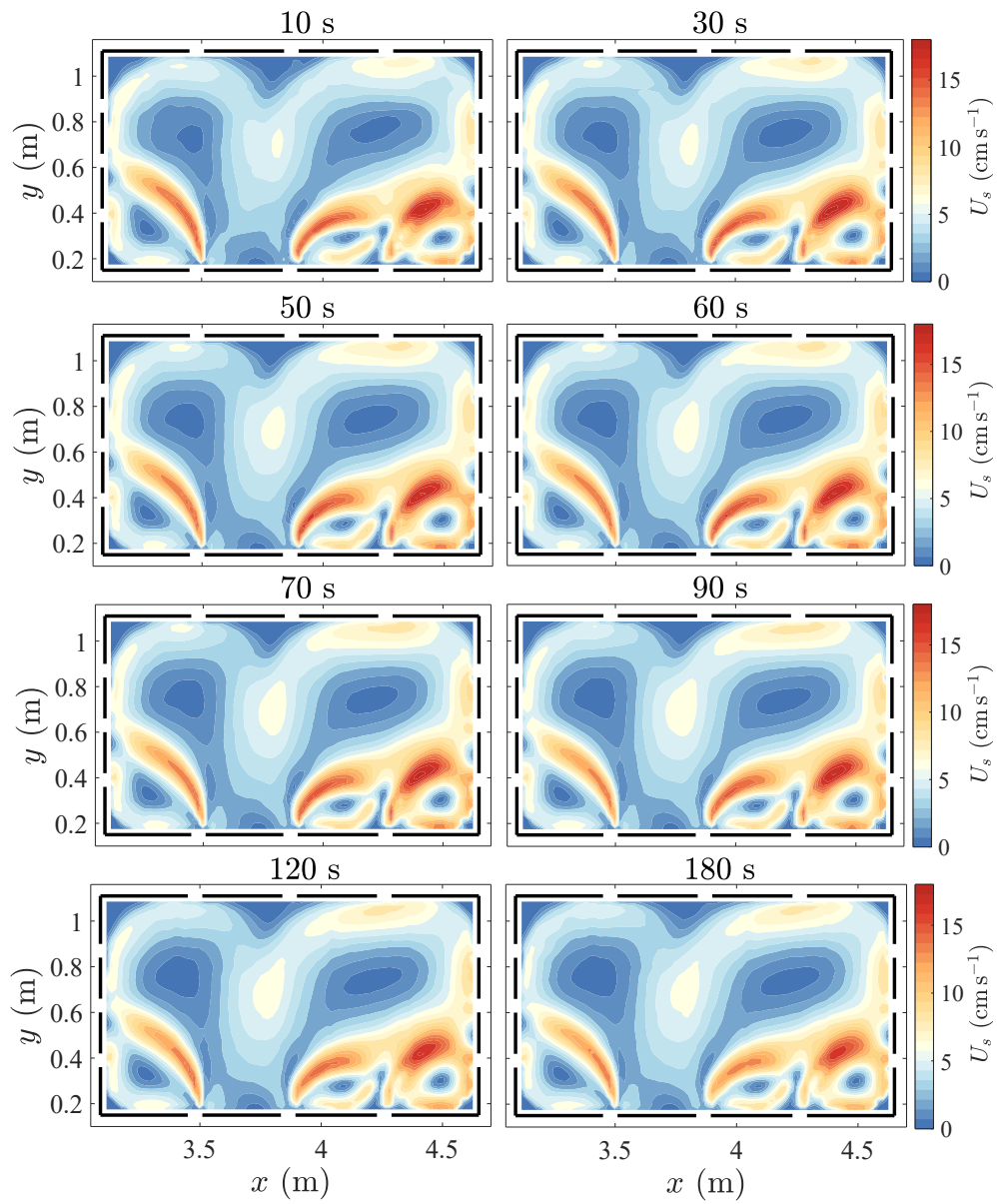


Figure A.14: Time-averaged surface velocity magnitude, U_s , within the urban block for increasing recording durations, from 10 s to 180 s, case C19-12.

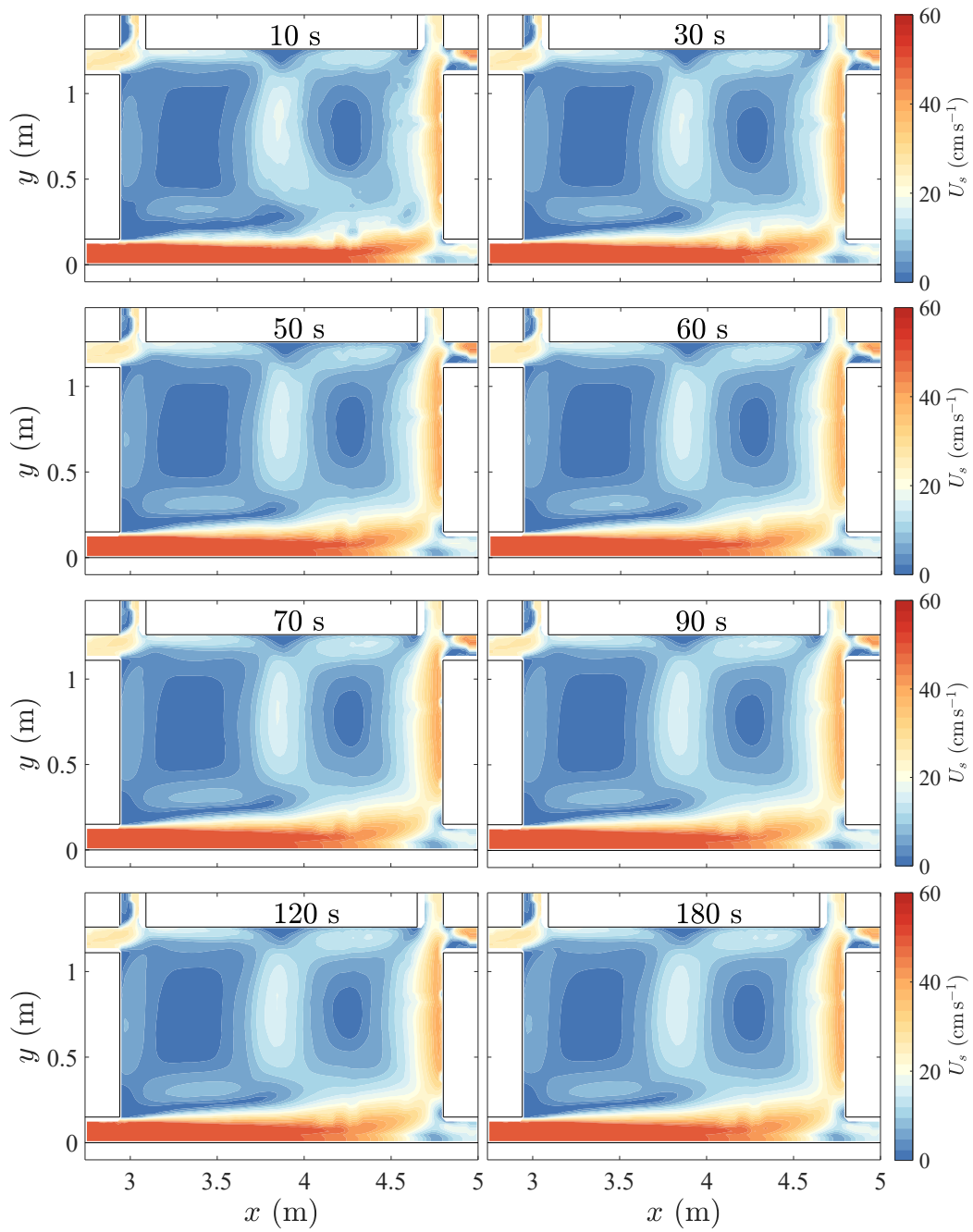


Figure A.15: Time-averaged surface velocity magnitude, U_s , for increasing recording durations, from 10 s to 180 s, case C100-100.

798 **Appendix B. Comparison between ADV and LSPIV velocity data**

799 *Appendix B.1. Velocities measured within the urban block*

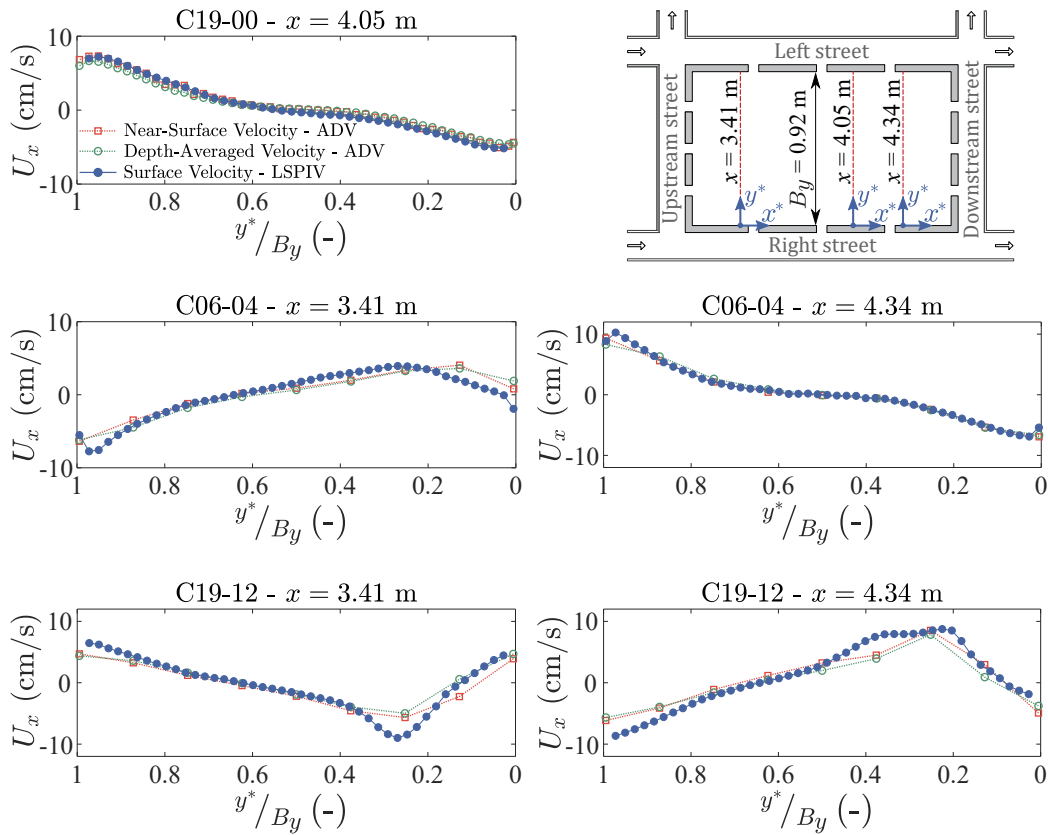


Figure B.16: Comparison of transverse profiles (along y -axis) of time-averaged velocity measured by LSPIV and ADV within the block for cases C19-00, C06-04 and C19-12. Two ADV velocities are plotted: in green the depth-averaged velocity and in red the velocity measured close to the free-surface. Local coordinates are denoted as x^* and y^* , as shown in the scheme on the top right.

800 *Appendix B.2. Velocities measured in the streets*

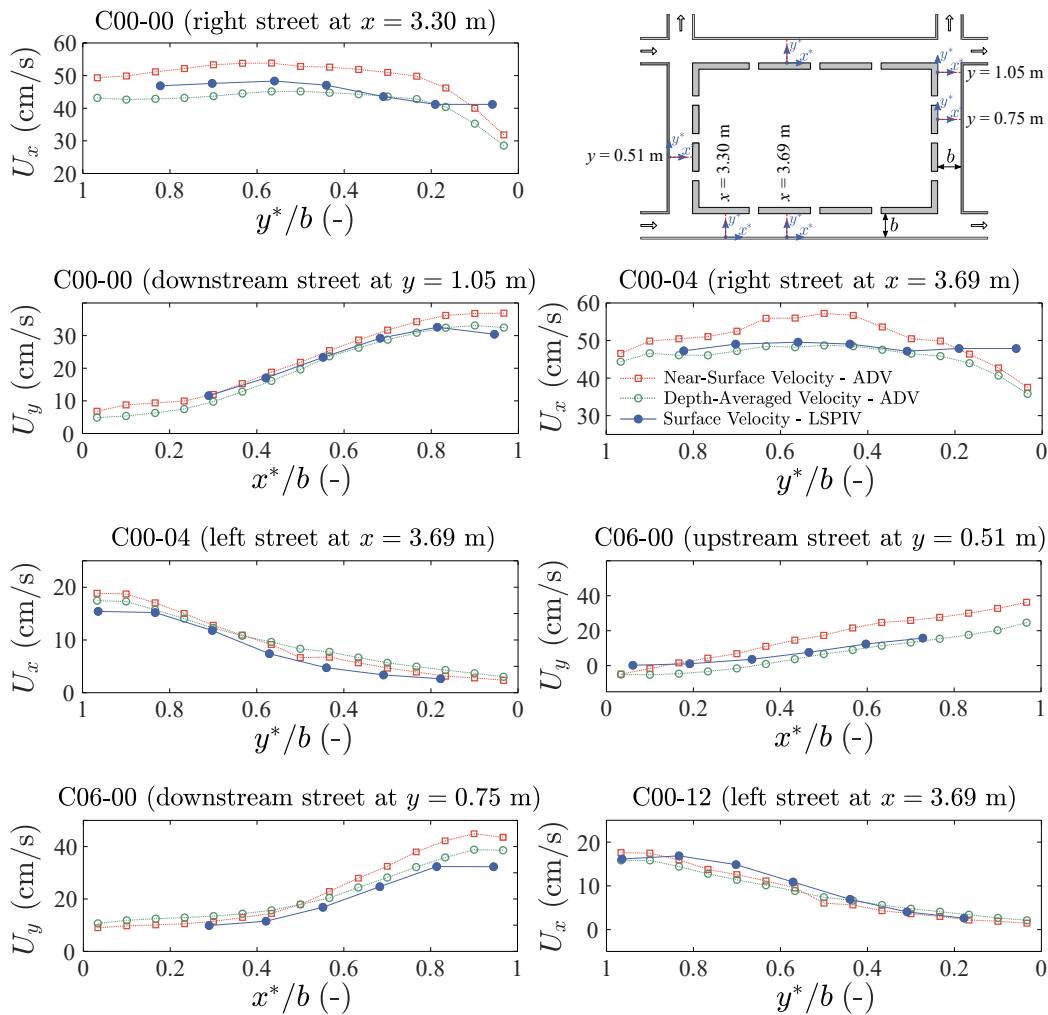


Figure B.17: Comparison of horizontal profiles of time-averaged streamwise velocity measured by LSPIV and ADV in the streets for cases C00-00, C00-04, C06-00 and C00-12. Two ADV velocities are plotted: in green the depth-averaged velocity and in red the velocity measured close to the free-surface. Local coordinates are denoted as x^* and y^* , as shown in the scheme on the top right.

801 **Appendix C. Impact of the extrapolation techniques on the dis-**
802 **charge estimate in the streets**

803 The computation of discharges in the streets with the velocity-area method
804 (Eqs. 1 and 2) requires an extrapolation of the measured velocity field at
805 the cross-sectional boundaries (bed, walls and free-surface). Due to the com-
806 plex flow patterns measured in the streets (mostly near the crossroads and
807 openings) distinct assumptions are required for this extrapolation. Three
808 conditions have been proposed: i) the *no-slip boundary condition* assumes
809 that the velocity of the fluid layer in direct contact with the boundary is
810 equal to the boundary velocity (Rapp, 2017), in this case $U = 0$, ii) the *slip*
811 *boundary condition* assumes a relative movement between the fluid layer and
812 the boundary, in this case it is assumed that the velocity at the boundary is
813 equal to the nearest velocity fluid, and iii) the *no-slip & slip boundary con-*
814 *dition* assumes an average of the previous two. Discharges computed using
815 these three conditions (from 0.5 l s^{-1} to 3.0 l s^{-1} in different streets) were com-
816 pared with the discharge readings given by the electromagnetic flowmeter. At
817 the free-surface, the slip boundary condition is systematically applied, while
818 for the other boundaries (bed and lateral walls), the appropriate condition
819 is selected according to the following criteria:

- 820 • No-slip boundary condition for the cross-sectional velocity distributions
821 where the largest velocity magnitude is concentrated in the center and
822 it decreases towards the boundaries, see Figure C.18.a, and where the
823 velocity over the entire flow depth is approximately the same, see Figure
824 C.18.b.

- 825 • No-slip & slip boundary condition for the cross-sectional velocity dis-
826 tributions where the velocity increases towards the boundaries, over at
827 least 50% of the surface, see Figure C.18.c.

- 828 • Slip boundary condition is not applied to the bed and walls. In all the
829 tests it was found that with this condition the discharge is significantly
830 overestimated, up to 14%.

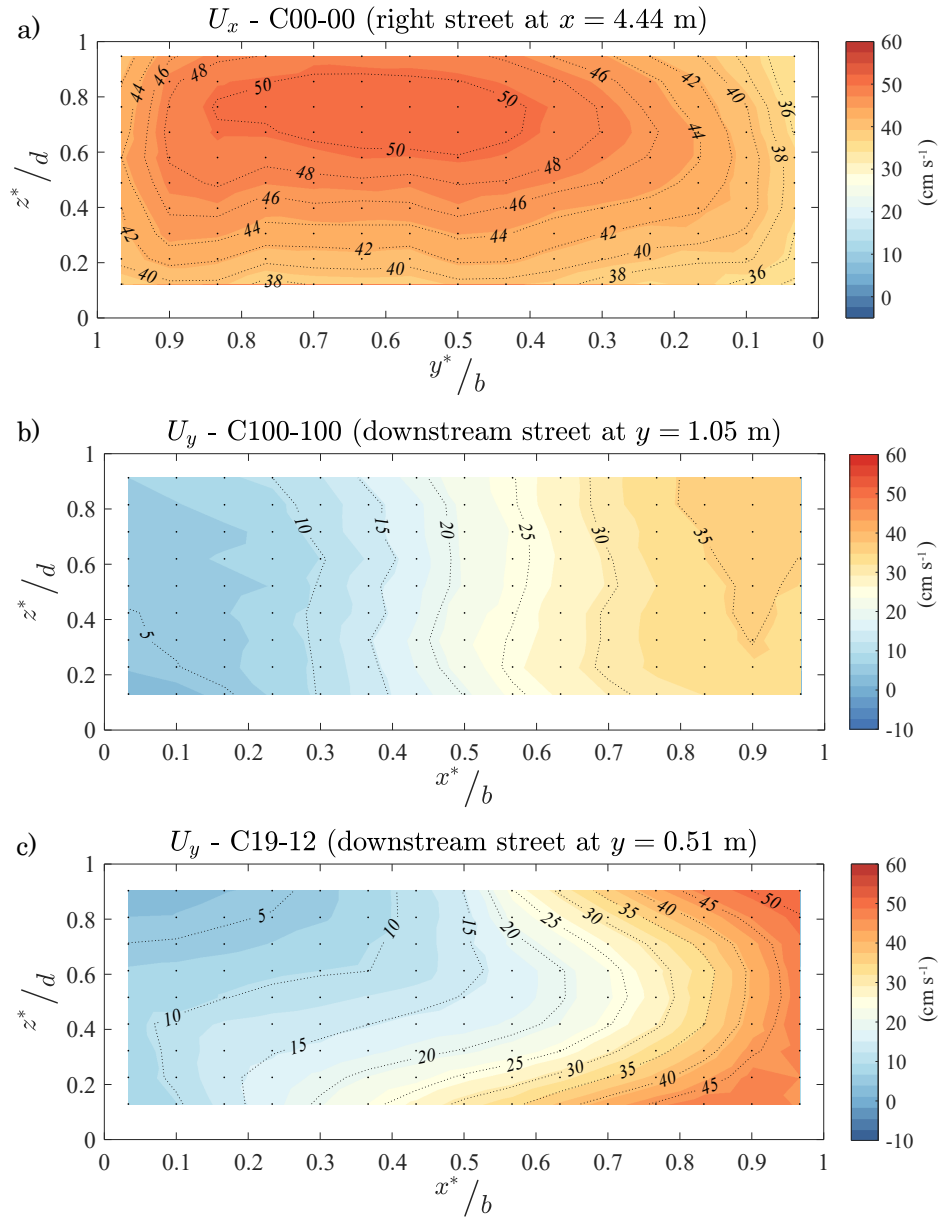


Figure C.18: Cross-sectional distribution of the time-averaged velocity for different cases: (a) and (b) are cross-sections where the discharge is computed assuming the non-slip condition, (c) where the discharge is computed assuming the average between no-slip and slip conditions.

831 **Appendix D. Additional experiments to study the impact of ur-**
832 **ban block porosity on the outlet discharge distribu-**
833 **tion.**

834 Table D.2 lists the additional experiments conducted to study the impact
835 of porosity on the outlet discharge distribution under different hydraulic and
836 geometric conditions (inflow distribution, longitudinal and transversal slopes
837 and height of weirs at the outlets). For each of the seven sets of experiments
838 (from A to G, with A being the set of experiments detailed in the paper)
839 four porosity cases were tested, three with a porous urban block: C00-04,
840 C00-12 and C19-12, and the reference case C00-00. Figure D.19 shows the
841 outlet discharge distribution as a percentage of the total inlet discharge for
842 all the sets, the bars indicate the average between the largest and smallest
843 values found among the 4 cases and the error bar indicates the variability
844 among these cases. With the variability, we can notice that for all the sets
845 the impact of the porosity on the outlet discharge distribution is relatively
846 low, the largest variation is $\pm 1.79\%$ at outlet 1 in the set of experiments F.

Table D.2: Characteristics of the additional sets of experiments. A is the original set of experiments in this paper.

Set of experiments	Height of the weir, w (cm)				Inflow (%) $Q_{in_1} - Q_{in_2}$	S_{0_x} (%)	S_{0_y} (%)
	Out 1	Out 2	Out 3	Out 4			
A	4	3	3	3	70 - 30	0.12	0.00
B	0	0	0	0			
C	0	0	0	0	90 - 10		
D	4	3	3	3	70 - 30	1.02	0.20
E	0	0	0	0			
F	4	3	3	3	90 - 10		
G	0	0	0	0			

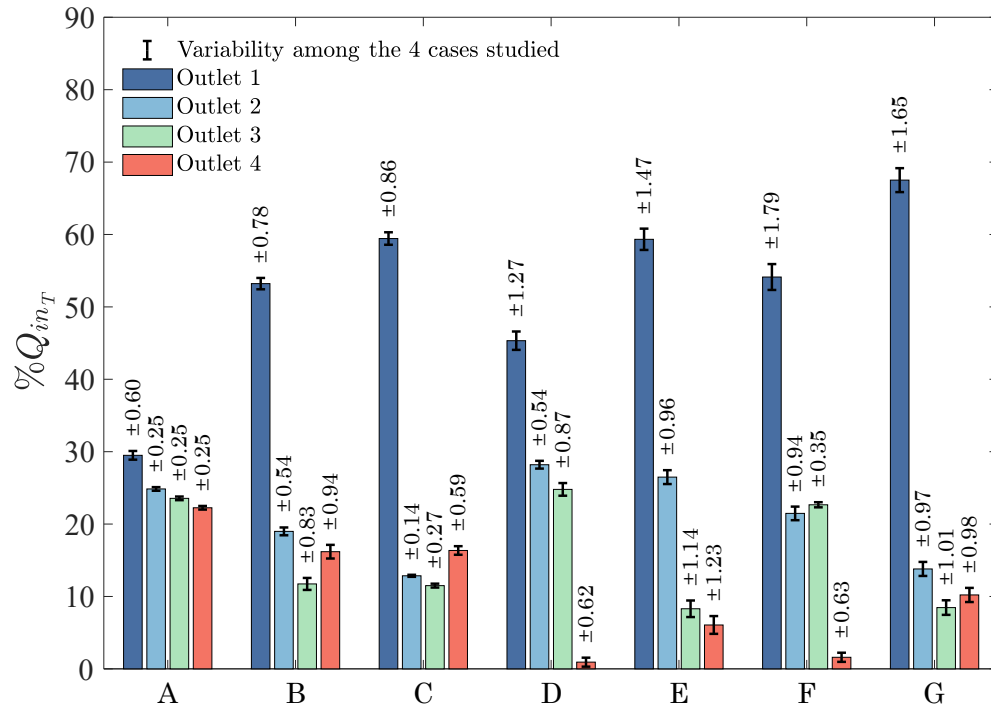


Figure D.19: Discharge distribution at the different outlets for each set of experiments, values shown as a percentage of the total inlet discharge ($Q_{in_T} = 6.5$ l/s.). The set of experiments A corresponds to the experiments detailed in the paper.